

Field of Junctions

Dor Verbin and Todd Zickler
Harvard University

{dorverbin, zickler}@seas.harvard.edu

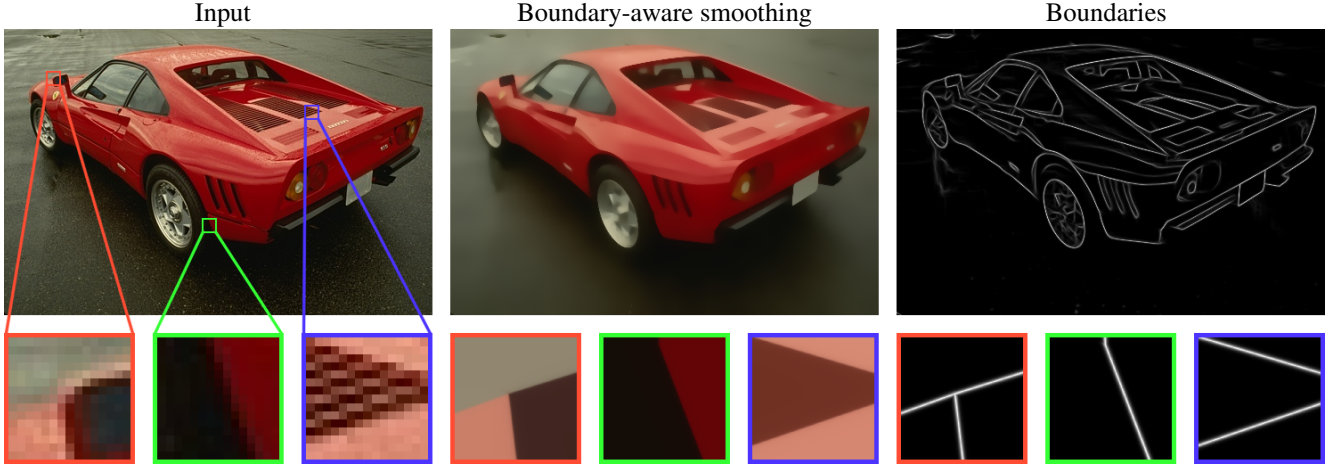


Figure 1: We explain every overlapping image patch—whether it contains a line, edge, corner, junction, or uniform color—as an instance of a generalized junction. Analyzing an image into its field of junctions provides useful boundary maps and boundary-aware smoothing as depicted here, and it is very insensitive to noise (see Figure 2). Image taken from [15].

Abstract

We introduce a bottom-up model for jointly finding many boundary elements in an image, including edges, curves, corners and junctions. The model explains boundary shape in each small patch using a junction with M angles and a freely-moving vertex. Images are analyzed by solving a non-convex optimization problem using purposefully-designed algorithms, cooperatively finding $M + 2$ junction values at every pixel. The resulting field of junctions is simultaneously an edge detector, a corner/junction detector, and a boundary-aware smoothing of regional appearance. We demonstrate how it behaves at different scales, and for both single-channel and multi-channel input. Notably, we find it has unprecedented resilience to noise: It succeeds at high noise levels where previous methods for segmentation and for edge, corner and junction detection fail.

1. Introduction

Identifying boundaries is fundamental to vision. It is helpful to be able to do it from the bottom up, because top-

down information about boundary-causing objects can be weak or unavailable. The essence of boundaries is easy to articulate: They are predominantly smooth and curvilinear; they include a small but important set of zero-dimensional events like corners and junctions; and in between boundaries, regional appearance is homogeneous in some sense.

Yet, despite the succinctness of this description, creating reliable boundary-finding algorithms that incorporate all of these attributes has proven to be hard. After decades of work on segmentation, edge detection, corner detection, junction detection, *etc.*, the community is still searching for succinct and comprehensive solutions. Even deep encoder-decoder CNNs, which can be highly tuned to exploit the non-local patterns of object shape and appearance in a dataset, struggle to localize boundary elements with precision, motivating the search for architectural innovations like skip connections, gated convolutions, bilateral regularization, multi-scale supervision, and so on.

We introduce a bottom-up model for boundaries that is surprisingly simple and effective. The model does not follow the common practice of analyzing images with linear filters. Instead, it explains every image patch as a (general-

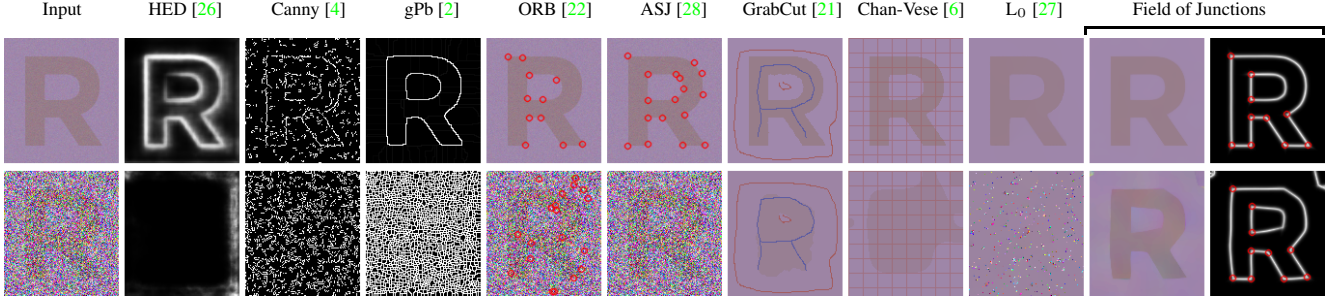


Figure 2: Analyzing the same image at low and high noise levels. From left to right: input image, boundary maps from edge detectors (HED, Canny, gPb); detections of corners or junctions superimposed on the input (ORB, ASJ); binary segmentations using manual initialization shown with thin lines (GrabCut, Chan-Vese) or without manual initialization (L_0); and output from the field of junctions. Existing approaches fail in the high noise regime, but the field of junctions does not.

ized) junction, and it analyzes an image through a cooperative, non-linear process that converges to a dense field of junction values defined at every pixel.

Analyzing an image into its field of junctions provides an intermediate representation of boundaries that is succinct and comprehensive. With only a handful of values at each pixel, the field of junctions provides a distilled representation of boundary structure in an image, including its edges, curves, corners, and junctions. It can be used for both single-channel and multi-channel images, naturally incorporating color information when it is available, and it can be used at different scales, with each scale providing a different amount of boundary detail. When applied to photographs, the field of junctions also provides “boundary-aware smoothing” as shown in Figure 1.

Our experiments show that a field of junctions is remarkably resilient. It is repeatable over a wide range of noise levels, including very high noise where other approaches—whether based on segmentation, edge detection, or corner/junction detection—all tend to fail. See Figure 2.

This paper begins by introducing the field of junctions model in Section 2, where we formulate analysis as a non-convex optimization problem. The section after that is the heart of the paper: It introduces the optimization techniques that allow analysis to succeed. In particular, we present a greedy algorithm for initializing each patch’s junction parameters that has convergence guarantees under certain conditions, and is very effective in practice even when the conditions do not hold. In Section 4 we apply the field of junctions to edge, corner, and junction detection, showing that it provides unparalleled repeatability across noise levels. We also demonstrate its behavior at different scales and with different values of its hyper-parameters (of which there are typically only two). Finally, in Section 5 we briefly discuss how the model relates to previous work.

2. Field of Junctions

Given an image $I: \Omega \rightarrow \mathbb{R}^K$, we extract from it a dense set of patches $\mathcal{I}_R = \{I_i(\mathbf{x})\}_{i=1}^N$, each of size $R \times R$. Let $\mathcal{P}_R = \{\mathbf{u}_\theta(\mathbf{x})\}$ be a continuous family of $R \times R$ patch-types, parametrized by θ , that describe the boundary structure within a patch. For \mathcal{P}_R we use the family of *generalized M -junctions*, which are comprised of M angular wedges around a vertex. The parameters $\theta = (\phi, \mathbf{x}^{(0)}) \in \mathbb{R}^{M+2}$ are M angles $\phi = (\phi^{(1)}, \dots, \phi^{(M)})$ and a 2-dimensional vertex position $\mathbf{x}^{(0)} = (x^{(0)}, y^{(0)})$. The vertex can be inside or outside of the patch, and some wedges may have size 0. Figure 3 shows examples for $M = 3$.

Let us assume that all image patches \mathcal{I}_R can be described by patches from \mathcal{P}_R with additive white Gaussian noise. This means that for every $i \in \{1, \dots, N\}$ there exist parameters θ_i and M color functions $c_i^{(1)}, \dots, c_i^{(M)}: \Omega_i \rightarrow \mathbb{R}^K$ (to be defined momentarily) such that for all $\mathbf{x} \in \Omega_i$:

$$I_i(\mathbf{x}) = \sum_{j=1}^M u_{\theta_i}^{(j)}(\mathbf{x}) c_i^{(j)}(\mathbf{x}) + n_i(\mathbf{x}), \quad (1)$$

where $n_i(\mathbf{x}) \sim \mathcal{N}(0, \sigma^2)$ is noise, and $u_{\theta_i}^{(j)}: \Omega_i \rightarrow \{0, 1\}$ is an indicator function that returns 1 if \mathbf{x} is inside the j th wedge defined by θ_i and 0 otherwise.

Each color function $c_i^{(j)}$ is defined over the support of the i th patch Ω_i and explains the continuous field of K -channel values within the j th wedge of that patch. These functions are constrained to a pre-chosen family of functions \mathcal{C} , such as constant functions $\mathcal{C} = \{c(\mathbf{x}) \equiv c: c \in \mathbb{R}^K\}$ or linear functions $\mathcal{C} = \{c(\mathbf{x}) = A\mathbf{x} + b: A \in \mathbb{R}^{K \times 2}, b \in \mathbb{R}^K\}$.

We write the process of analyzing an image into its field of junctions as solving the optimization problem:

$$\hat{\Theta} = \underset{\Theta}{\operatorname{argmax}} \log p(\Theta) + \sum_{i=1}^N \log p(I_i | \theta_i; \mathbf{c}_i), \quad (2)$$

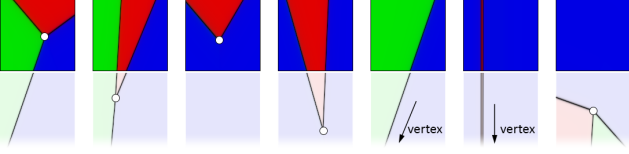


Figure 3: Our generalized junction comprises a vertex and M angles, partitioning each patch into at most M uniform regions (here, $M = 3$). By freeing the vertex to be variously inside or outside of patches as needed, the model simultaneously accommodates edges, lines, corners, junctions, and uniform regions, thereby allowing concurrencies between all of them to be exploited during analysis.

where $p(\Theta)$ is a spatial consistency term over all junction parameters $\Theta = (\theta_1, \dots, \theta_N) \in \mathcal{P}_R^N$, and $p(I_i | \theta_i; \mathbf{c}_i)$ is the likelihood of a patch I_i given the junction parameters θ_i and parametrized by color functions $\mathbf{c}_i = (c_i^{(1)}, \dots, c_i^{(M)})$. In the low-noise regime, this objective is the MAP estimate of the field of junctions, where the consistency term $p(\Theta)$ is interpreted as the prior over the junction parameters.

For each patch i finding the optimal color functions given the junction parameters is trivial. For the case of a piecewise constant color model they are

$$c_i^{(j)} = \frac{\int u_{\theta_i}^{(j)}(\mathbf{x}) I_i(\mathbf{x}) d\mathbf{x}}{\int u_{\theta_i}^{(j)}(\mathbf{x}) d\mathbf{x}}, \quad (3)$$

and for the piecewise linear model, a similar closed form expression for $c_i^{(j)}(\mathbf{x}) = A_i^{(j)}\mathbf{x} + b_i^{(j)}$ can be obtained with very little increased computation by replacing each of the K divisions in Equation 3 with a 3×3 matrix inversion and multiplication by a 3-vector.

Most of our experiments are done using the piecewise constant 3-junction model, but in Section 4 we discuss the advantages of using a junction model with $M > 3$.

2.1. Patch Likelihood

For a single patch, Equation 1 directly shows that the log-likelihood term is negatively proportional to the mean squared error in that patch:

$$\log p(I_i | \theta_i; \mathbf{c}_i) = -\alpha \sum_{j=1}^M \int u_{\theta_i}^{(j)}(\mathbf{x}) \|I_i(\mathbf{x}) - c_i^{(j)}\|^2 d\mathbf{x}, \quad (4)$$

where the colors are determined using the junction parameters as in Equation 3, and $\alpha > 0$ is a constant determined by the noise level σ .

The likelihood term in Equation 4 depends only on the junction parameters at a single location, θ_i . Despite the low dimensionality of the problem, which requires estimating a single 5-dimensional junction parameter per patch (in the

case of 3-junctions), finding the optimal junction parameters is a substantial challenge. We present an efficient solution to this problem in Section 3.1.

2.2. Spatial Consistency

Our spatial consistency term $p(\Theta)$ requires that all junction models agree within their overlap. This condition can be succinctly written as a constraint on the boundaries defined by each junction:

$$\log p(\Theta) = \begin{cases} 0 & \text{if } B_i(\mathbf{x}) = B(\mathbf{x}) \text{ for all } i \\ -\infty & \text{otherwise} \end{cases}, \quad (5)$$

where $B_i(\mathbf{x})$ is the *boundary function* at the i th patch that returns 1 if \mathbf{x} is a boundary location according to θ_i and 0 otherwise, and $B(\mathbf{x}) = \max_{i \in \{1, \dots, N\}} B_i(\mathbf{x})$ is the *global boundary function* defined by the entire field of junctions.

The consistency term in Equation 5 provides a hard constraint on the junction parameters, which is difficult to use in practice. We instead replace it with a relaxed, finite version having width δ and strength β :

$$\log p(\Theta) = -\beta \sum_{i=1}^N \int [B_i^{(\delta)}(\mathbf{x}) - B^{(\delta)}(\mathbf{x})]^2 d\mathbf{x}, \quad (6)$$

where $B_i^{(\delta)}(\mathbf{x})$ is a smooth boundary function with dropoff width δ from the exact boundary position, to be defined precisely in Section 3.2. $B^{(\delta)}(\mathbf{x})$ is a relaxed global boundary function computed by averaging the smooth local boundary function for each position \mathbf{x} over all patches containing it:

$$B^{(\delta)}(\mathbf{x}) = \frac{1}{|N_{\mathbf{x}}|} \sum_{i \in N_{\mathbf{x}}} B_i^{(\delta)}(\mathbf{x}), \quad (7)$$

where $N_{\mathbf{x}} = \{i: \mathbf{x} \in \Omega_i\}$ is the set of indices of patches that contain \mathbf{x} . See examples for the global and local boundary functions in Figure 1. Note that the relaxed consistency in Equation 6 approaches the strict one from Equation 5 when $\delta \rightarrow 0$ and $\beta \rightarrow \infty$.

Using the expressions for the log-likelihood and the relaxed consistency in Equations 4 and 6, analyzing an image into its field of junctions can now be written as the solution to the following minimization problem:

$$\begin{aligned} \argmin_{\Theta \in \mathcal{P}_R^N} & \sum_{i=1}^N \sum_{j=1}^M \int u_{\theta_i}^{(j)}(\mathbf{x}) \|I_i(\mathbf{x}) - c_i^{(j)}\|^2 d\mathbf{x} \\ & + \lambda \sum_{i=1}^N \int [B_i^{(\delta)}(\mathbf{x}) - B^{(\delta)}(\mathbf{x})]^2 d\mathbf{x}, \end{aligned} \quad (8)$$

where $\lambda = \beta/\alpha$ is a parameter controlling the strength of consistency, and the optimal regional appearance values

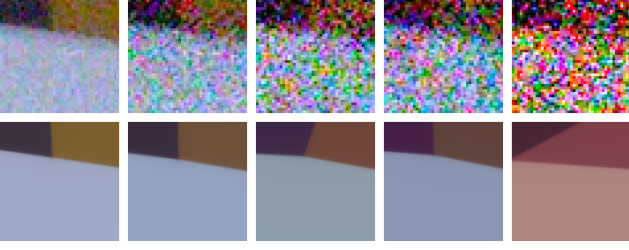


Figure 4: The result of Algorithm 2 on a single patch extracted from images from SIDD captured by smartphone cameras with decreasing light levels. While our algorithm is only guaranteed to converge when the input image has no noise, it obtains a good estimate even when noise levels are very high.

$\{\mathbf{c}_i^{(j)}\}$ are determined from Θ using Equation 3 (or analogous closed-form expressions for piecewise-linear or other color function families).

Our formulation of consistency encourages each patch i to agree with its overlapping neighbors, by inhibiting its own boundariness $B_i^{(\delta)}(\mathbf{x})$ at pixels \mathbf{x} that are assigned a low score by their neighbors (as quantified by $B^{(\delta)}(\mathbf{x})$) and exciting it at pixels assigned a high score. This means that only salient junctions, corners, edges and lines end up contributing to the final global boundary map $B^{(\delta)}(\mathbf{x})$. The junction values in uniform patches and other patches that have no salient boundary signal tend to disagree with the junction values of other patches, so spurious boundaries within them tend to be suppressed. At the same time, our use of a smoothed version of consistency instead of a strict one allows for boundaries with nonzero curvature to be well approximated by local collections of corners that have slightly different vertices.

3. Analysis

Analyzing an image into its field of junctions is a challenge, with Problem (8) consisting of N junction-fitting problems that are coupled by spatial consistency. Even without consistency, finding the optimal junction for a single patch i requires minimizing a non-smooth and non-convex function in θ_i .

We solve the problem in two parts: initialization and refinement. Both of these are key to our model’s robustness to noise. The initialization procedure independently optimizes each patch, using a handful of coordinate updates to find discrete values for its angles and vertex location. Then, the refinement procedure performs gradient descent on a relaxation of Problem (8), cooperatively adjusting all junction parameters to find continuous angles and sub-pixel vertex locations that improve spatial consistency while maintaining fidelity to local appearance. We describe each step separately.

3.1. Initialization

Many previous methods for junction estimation, such as [7, 5], use gradient descent to optimize the vertex and angles of a single wedge model. These methods rely on having a good initialization from a human or a corner detector, and they fail when such initializations are unavailable. Indeed, even in the noiseless case, there always exists an initialization of a patch’s junction parameters around which the negative log-likelihood is locally constant.

In the present case, we need an initialization strategy that is automatic and reliable for *every* patch, or at least the vast majority of them. We first describe an initialization algorithm for the simpler problem in which the vertex of a patch is known, where our algorithm guarantees optimality in the absence of noise; and then we expand it to solve for the vertex and angles together.

When the vertex is known, optimizing the parameters of one patch reduces to finding a piecewise-constant, one-dimensional angular function. There are algorithms for this based on dynamic programming [11] and heuristic particle swarm optimization [3]. We instead propose Algorithm 1, which is guaranteed to find the true junction angles $\phi = (\phi^{(1)}, \dots, \phi^{(M)})$ that minimize the negative log-likelihood $\ell(\phi, \mathbf{x}^{(0)}) = -\log p(I_i | \theta; \mathbf{c}_i)$ in the noiseless case. The algorithm consists of a single coordinate-descent update over the M junction angles, that is, it minimizes $\ell_j(\phi) \triangleq \ell(\phi^{(1)}, \dots, \phi^{(j-1)}, \phi, \phi^{(j+1)}, \dots, \phi^{(M)}, x^{(0)}, y^{(0)})$ for $j = 1, \dots, M$.

Algorithm 1: Optimization of angles

```

Initialize  $\phi^{(1)}, \dots, \phi^{(M)} \leftarrow 0$ .
for  $j = 1, \dots, M$  do
     $\phi^{(j)} \leftarrow \underset{\phi}{\operatorname{argmin}} \ell_j(\phi)$ 
end
```

Theorem 1. For a junction image $I_i(\mathbf{x})$ with no noise (i.e., $n_i \equiv 0$ in Eq. 1) and with vertex $\mathbf{x}^{(0)}$ known, Algorithm 1 is guaranteed to find the globally optimal angles ϕ .

The full proof of Theorem 1 is in the supplement, and we provide a proof sketch here.

Proof Sketch. First, note that $\ell_j(\phi)$ is continuous and smooth for all ϕ other than possibly a discontinuity in the derivative at any of the true junction angles. If the optimal ϕ is not one of the true junction angles then it must lie in the *open* interval between two such angles, i.e. $\phi \in (\phi^-, \phi^+)$. It can be shown (see supplement for more details) that $\ell_j(\phi)$ does not have any local minima in (ϕ^-, ϕ^+) , and therefore for each angular interval between two true junction angles the cost function must be minimized at one of the endpoints. Therefore repeatedly minimizing $\ell_j(\phi)$ for $j = 1, \dots, M$ is guaranteed to provide a globally optimal set of angles. \square

In practice, we find that Algorithm 1 provides an excellent estimate of the true junction angles even when the input patch is noisy. It also has an efficiency advantage. Each coordinate update can be done to an arbitrarily small error ε with complexity $O(1/\varepsilon)$, by exhaustively searching over all angles in increments of ε . The complexity for a single junction is therefore $O(M/\varepsilon)$, in contrast with the $O(1/\varepsilon^2)$ dynamic programming solution of [11] and the $O(1/\varepsilon^M)$ of naive exhaustive search over all possible M -angle sets. Moreover, each step of the algorithm can be trivially run in parallel over all angles (and over all patches) by computing the value of $\ell_j(\phi^{(j)})$ for each of the $O(1/\varepsilon)$ values and choosing the minimizing angle. Thus, runtime can be accelerated significantly using a GPU or multiple processors.

These efficiency advantages become especially important when we expand the problem to optimize the vertex in addition to the angles. We simply do this by initializing the vertex at the center of the patch and updating it along with the angles using an iterative discrete coordinate descent. See Algorithm 2. Figure 4 shows a typical example, where the algorithm results in a good estimate of the true vertex position and angles even when there is a substantial amount of noise.

Algorithm 2: Optimization of angles and vertex

Initialize $x^{(0)}, y^{(0)}$ at the center of the patch.

for $i = 1, \dots, N_{\text{init}}$ **do**

 Find angles ϕ using Algorithm 1.

$x^{(0)} \leftarrow \underset{x}{\operatorname{argmin}} \ell(\phi, x, y^{(0)})$

$y^{(0)} \leftarrow \underset{y}{\operatorname{argmin}} \ell(\phi, x^{(0)}, y)$

end

3.2. Refinement

After initializing each patch separately, we refine the field of junctions using continuous, gradient-based optimization. In order to compute the gradient of the objective in Problem (8) with respect to Θ we relax the indicator functions $\{\mathbf{u}_\theta(\mathbf{x})\}$, making them smooth in \mathbf{x} and in θ , similar to level-set methods [6, 24]. We do this by describing each 3-junction using two distance functions (a similar parametrization exists using $M - 1$ functions for M -junctions). Given the vertex position $(x^{(0)}, y^{(0)})$ and angles $\phi^{(1)}, \phi^{(2)}, \phi^{(3)}$, and assuming without loss of generality that $0 \leq \phi^{(1)} \leq \phi^{(2)} \leq \phi^{(3)} < 2\pi$, we define a junction using two distance functions d_{12} and d_{13} defined by:

$$d_{kl}(\mathbf{x}) = \begin{cases} \min\{d_k(\mathbf{x}), -d_l(\mathbf{x})\} + \tau_{kl} & \text{if } \phi_l - \phi_k < \pi \\ \max\{d_k(\mathbf{x}), -d_l(\mathbf{x})\} + \tau_{kl} & \text{otherwise} \end{cases} \quad (9)$$

where $d_l(x, y) = -(x - x^{(0)}) \sin(\phi^{(l)}) + (y - y^{(0)}) \cos(\phi^{(l)})$ is the distance function from a line with angle $\phi^{(l)}$ pass-



Figure 5: Non-photorealistic editing by combining the smoothed image (Eq. 14) and the boundary map (Eq. 7) obtained from the field of junctions. Image taken from [15].

ing through $(x^{(0)}, y^{(0)})$, and $\tau_{kl} = \tau \cdot g\left(\frac{\phi^{(l)} - \phi^{(k)}}{\pi} - 1\right)$, with parameter τ and a monotonically increasing function $g : [-1, 1] \rightarrow [-1, 1]$ used for smoothing the transition between a corner and a uniform patch, *i.e.* in the cases where $\phi^{(l)} - \phi^{(k)}$ is close to 0 or 2π . When the angle $\phi^{(l)} - \phi^{(k)}$ approaches 0 we want $\tau_{kl} \approx -\tau < 0$; when it approaches 2π we want $\tau_{kl} \approx \tau > 0$; and when it is far from both we want $\tau_{kl} \approx 0$. Our choice is to use $g(\phi) = \phi^m$ for some large odd integer m , which we set to $m = 35$.

Our relaxed indicator functions are defined as:

$$\begin{aligned} u_\theta^{(1)}(\mathbf{x}) &= 1 - H_\eta(d_{13}(\mathbf{x})), \\ u_\theta^{(2)}(\mathbf{x}) &= H_\eta(d_{13}(\mathbf{x})) [1 - H_\eta(d_{12}(\mathbf{x}))], \\ u_\theta^{(3)}(\mathbf{x}) &= H_\eta(d_{13}(\mathbf{x})) H_\eta(d_{12}(\mathbf{x})), \end{aligned} \quad (10)$$

where H_η is the regularized Heaviside function, as in [6]:

$$H_\eta(d) = \frac{1}{2} \left[1 + \frac{2}{\pi} \arctan\left(\frac{d}{\eta}\right) \right]. \quad (11)$$

The smooth boundary maps for the consistency term are:

$$B_i^{(\delta)}(\mathbf{x}) = \pi\delta \cdot H'_\delta(\min\{|d_{12}(\mathbf{x})|, |d_{13}(\mathbf{x})|\}), \quad (12)$$

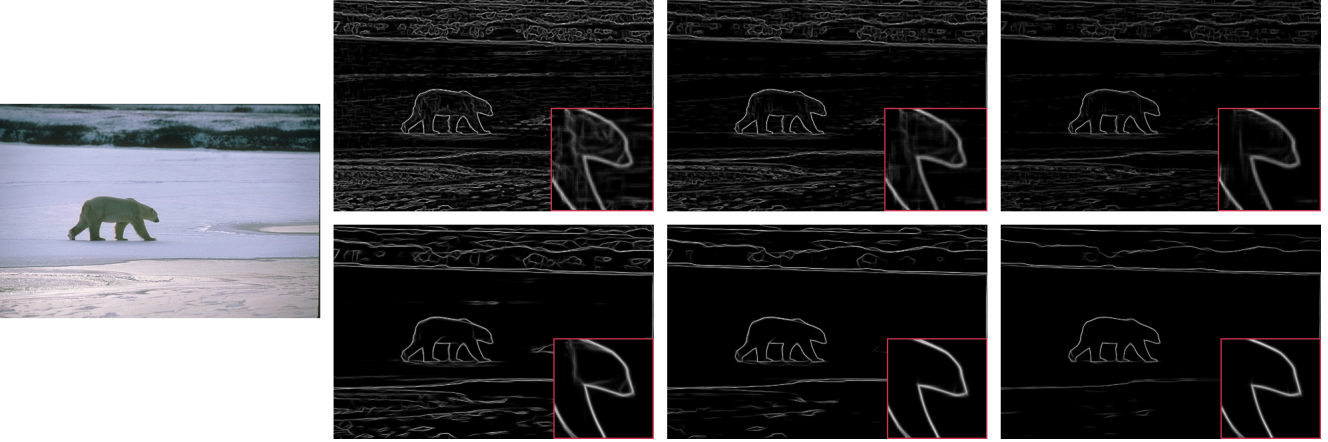


Figure 6: Effect of the two model parameters. Patch size R (top: 7, bottom: 15) controls the scale of the details captured by the field of junctions, while consistency weight λ (from left to right: 0.05, 0.2, and 0.5) controls level of detail at that scale.

where $H'_\delta(d)$ is the derivative of $H_\delta(d)$ with respect to d , and the scaling factor ensures that $0 \leq B_i^{(\delta)}(\mathbf{x}) \leq 1$.

In all of our experiments we set $\tau = 0.1$, $\eta = 0.01$ and $\delta = 0.1$. We find that the algorithm is fairly insensitive to the choice of these values, and that varying them does not provide useful control of the model’s behavior. This is in contrast to the other parameters—patch size R and consistency weight λ —that control scale and level of detail as will be shown in Section 4.

3.3. Optimization Details

We analyze an image into its field of junctions by first initializing with Algorithm 2 for $N_{\text{init}} = 30$ iterations, followed by refinement to minimize Equation 8 using the Adam optimizer [12] for $N_{\text{iter}} = 1000$ iterations. Initialization is performed by evaluating the restricted negative log-likelihood functions in Algorithms 1 and 2 at 100 different values. Because the vertex of a junction can be outside its patch (see Figure 3), each of its two coordinates is searched over an interval of length $3R$ around the center of each patch. The precision of our initialization is therefore 3.6° in the junction angles, and $0.03R$ in the vertex position.

For the refinement step we use a learning rate of 0.03 for the vertex positions and 0.003 for the junction angles. In order to allow the parameters to first improve their estimates locally and only then use the consistency term to improve the entire field of junctions, we linearly increase the consistency weight from 0 to its final value λ over the 1000 refinement iterations. Our algorithm is implemented in PyTorch, and its runtime is approximately 2 minutes on a 250×250 image using an NVIDIA Tesla V100 GPU.

4. Experiments

Once an image is analyzed, its field of junctions provides a rich, distributional representation of boundary structure and smooth regional appearance. Each pixel in the field essentially provides a “vote” for a nearby (sub-pixel) vertex location and associated collection of wedge angles around that location. Here we show that simple pixel-wise averages that are derived from the field are useful for boundary detection, corner and junction detection, and image editing.

We evaluate performance using three sources of data. The first is our own dataset of 300 synthetic grayscale images, some of which are shown in the supplement. They allow complete control of noise levels, and they contain boundary lines, curves, corners, and junctions whose locations are known to high sub-pixel precision. The second source of data is the Smartphone Image Denoising Dataset (SIDD) [1], which provides color images captured under low-light conditions with varying amounts of noise as well as clean ground-truth. Third, we show qualitative image editing results on a small number of photographs from the BSD [15]. We compare our results to the related prior work in edge detection, corner detection, and junction detection as appropriate. In our quantitative evaluations, we report noise levels using peak signal to noise level (PSNR) in dB, which is the inverse of the mean squared error between the noisy image and the noiseless ground truth that is normalized to have unitary maximum value. Lower PSNR values indicate higher noise, and $\text{PSNR} = \infty$ when noise is absent.

Boundary Detection. A field of junctions immediately provides a boundary map via Equation 7. Figure 1 shows the resulting boundaries extracted from a photograph, and Figure 2 shows a qualitative comparison of our boundaries to previous edge detection and segmentation methods. Fig-

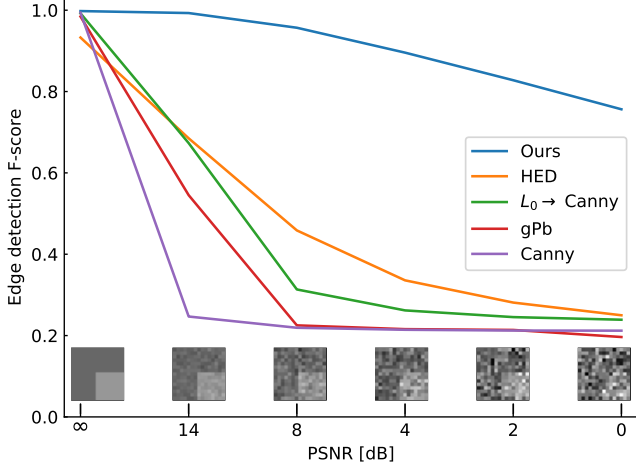


Figure 7: Boundary detection F-score for increasing noise on our dataset. Our model is comparable to other edge detectors at low noise but outperforms them significantly at high noise. Insets: sample patch at different noise levels.

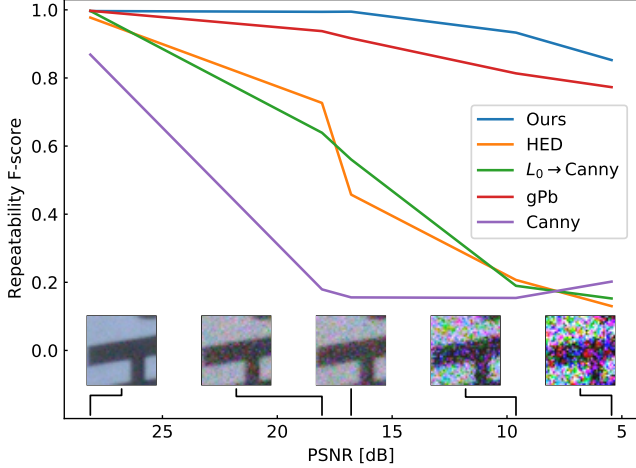


Figure 8: Repeatability of boundary detection over increasing noise levels using patches extracted from low-light smartphone images in SIDD [1]. The F-score is computed by comparing the edges detected by each method in a noisy image to those detected in the noiseless ground truth image. Insets: sample patches at different noise levels.

ure 6 demonstrates the effect of the two parameters of our model: increasing the patch size R increases the scale of the details captured by the field of junctions, while increasing λ removes the less salient details at the scale selected by R .

We quantitatively compare our results to existing edge and boundary detection methods: gPb [2], HED [26], Canny [4], and Canny applied to the result of L_0 smoothing [27]. In Figure 7 we show the F-scores of results obtained by each method on our synthetic dataset. The F-score is computed by matching the boundaries output by

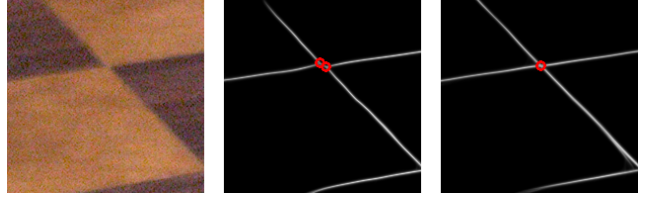


Figure 9: Close-up of the output of our model with $M = 3$ (center) and with $M = 4$ (right) on an image from SIDD. Here, the latter allows for better localization of the X-junction and the boundaries in its neighborhood.

each detector with the ground truth and taking the harmonic mean of its precision and recall, as in [15]. Figure 8 shows the repeatability of each detector over different noise levels using patches extracted from SIDD. The repeatability F-scores are computed by comparing the boundary map obtained by each method on the noisy images with its output on the noiseless ground truth images. In all cases we find that our model provides superior resilience to noise.

Vertex Detection. In addition to a boundary map, a field of junctions provides a map of vertex locations that can be used like a traditional corner, junction, or interest point detector. To create the vertex map, we use simple weighted voting from each pixel in the field of junctions, estimating the likelihood that location \mathbf{x} contains a vertex using:

$$V(\mathbf{x}) = \sum_{i=1}^N w_i \kappa(\mathbf{x} - \mathbf{x}_i^{(0)}), \quad (13)$$

with a Gaussian kernel $\kappa(\Delta\mathbf{x}) = \exp\left(-\frac{\|\Delta\mathbf{x}\|^2}{2\gamma^2}\right)$ having width γ , and with weights $\{w_i\}$ designed to suppress votes cast by pixels whose junction angles are all close to 0° or 180° (corresponding to junctions with no unique vertex), or by pixels whose junction vertex $\mathbf{x}^{(0)}$ is very far from the center of the patch (see supplement for the full expression).

Figure 2 shows the qualitative results of our vertex detector in the low- and high-noise regime, compared with previous interest point and junction detectors. A quantitative study of the robustness of our detector to noise on our synthetic dataset is shown in Figure 10. We again use F-score to compare to Harris [8], ASJ [28], and to baseline CNNs that we trained on our dataset specifically for vertex detection. In this experiment, each of the CNNs was trained and tested on subsets of images having the same PSNR. Figure 11 shows the repeatability of our vertex detector over increasing noise on SIDD, analogous to the similar experiment for boundaries above. Again we find that our model provides the advantage of being highly resilient to noise. Our detector also provides repeatability over change in viewpoint angle similar to other interest point detectors (see supplement for more details).

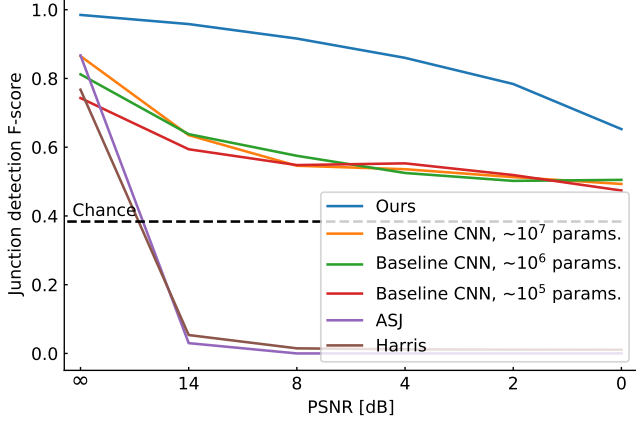


Figure 10: Vertex detection F-score for increasing noise on our dataset. Our model performs similarly to a baseline CNN and to other corner and junction detectors (Harris, ASJ) at low noise, but outperforms them at high noise. See Fig. 7 for sample patches.

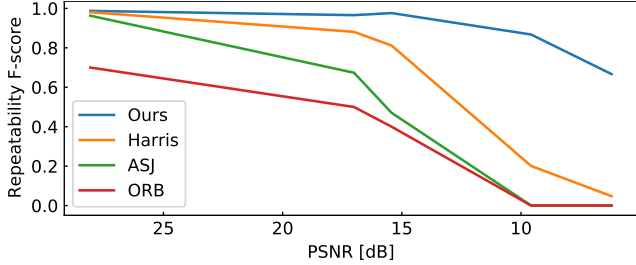


Figure 11: Vertex detection repeatability over increasing noise on patches from SIDD, compared to repeatability of other detectors. See Fig. 8 for sample patches. The number of points detected by each method on the clean ground truth is 126 (ours), 49 (ASJ), 57 (Harris), and 70 (ORB).

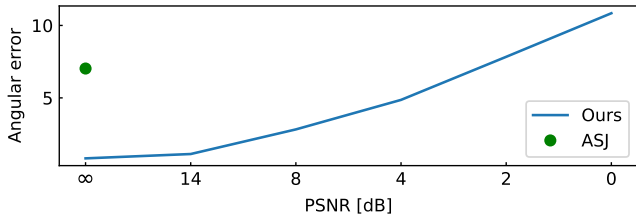


Figure 12: Error of angles (in degrees) at detected junctions on our dataset, for our method and ASJ. Our method degrades slowly. Because ASJ fails at moderate noise (see Fig. 10), we report its accuracy on clean images, only using correctly-detected junctions. See Fig. 7 for sample patches.

In addition to the vertex locations, a field of junctions provides an estimate of the angles of each detected vertex. For this we simply use ϕ_i as an estimate for the angles at a pixel i . Figure 12 shows a comparison of this angle estimation accuracy over multiple noise levels with ASJ. Because

ASJ fails at moderate noise levels (see Figure 10), we only plot its error on clean images where its detection succeeds.

Figure 9 demonstrates how our model behaves when applied using $M = 4$ angles per pixel instead of $M = 3$. Including a fourth angle adds the ability to represent X-junctions, which appear on checkerboards like this example and are common in scenes with transparency [17].

Image Editing. Finally, a field of junctions also provides a boundary-aware smoothing of an image. We compute this by averaging the color functions defined in Equation 3:

$$\hat{I}(\mathbf{x}) = \frac{1}{|N_{\mathbf{x}}|} \sum_{i \in N_{\mathbf{x}}} \sum_{j=1}^M u_i^{(j)}(\mathbf{x}) \mathbf{c}_i^{(j)}(\mathbf{x}). \quad (14)$$

An example is shown in Figure 1, and in Figure 5 we show an artistic effect obtained by combining the smoothed image with the boundary map.

5. Relation to Previous Approaches

To close the paper, we briefly describe how the field of junctions relates to analysis strategies that came before it.

Encoder/decoder networks. Deep convolutional networks with pooled intermediate features that are trained on large datasets can provide top-down contextual information about object shape that informs the locations of edges and junctions (e.g., [26, 10]). However, the spatial subsampling in these architectures makes boundaries hard to localize. The field of junctions is a different type of intermediate feature that is not subsampled. It would complement the learned intermediate features of a CNN.

Edge, corner, and junction detection. These have been studied for decades, often separately, using halved circular windows to analyze edges [4, 2], and wedges or other models for corners and junctions [8, 20, 7, 14, 5, 25, 28]. The major disadvantage of this strategy is that it does not exploit concurrency between edges, corners and junctions at detection time. In contrast, our generalized junction model accommodates edges, lines, corners, junctions and uniform regions simultaneously, allowing all of these signals to mutually excite and inhibit during analysis.

Segmentation. Our junction model is inspired by the level-set method of Chan and Vese [6] and in particular its multi-phase generalizations [24, 9]. In fact, our descent strategy in Section 3.2 can be interpreted as pursuing optimal level-set functions in each patch, with each patch’s functions constrained to a continuous $(M + 2)$ -parameter family. Our experiments show that this patch-wise approach obviates the need for manually initializing the level set functions over the image plane and for re-initializing them during optimization, both of which have been perennial limitations in practice [6, 24, 9, 13].

References

- [1] Abdelrahman Abdelhamed, Stephen Lin, and Michael S Brown. A high-quality denoising dataset for smartphone cameras. In *Proceedings of the IEEE Conference on Computer Vision and Pattern Recognition*, pages 1692–1700, 2018. 6, 7
- [2] Pablo Arbelaez, Michael Maire, Charless Fowlkes, and Jitendra Malik. Contour detection and hierarchical image segmentation. *IEEE transactions on pattern analysis and machine intelligence*, 33(5):898–916, 2010. 2, 7, 8
- [3] Leif Bergerhoff, Joachim Weickert, and Yehuda Dar. Algorithms for piecewise constant signal approximations. In *2019 27th European Signal Processing Conference (EUSIPCO)*, pages 1–5. IEEE, 2019. 4
- [4] John Canny. A computational approach to edge detection. *IEEE Transactions on pattern analysis and machine intelligence*, (6):679–698, 1986. 2, 7, 8
- [5] Miguel A Cazorla and Francisco Escolano. Two Bayesian methods for junction classification. *IEEE Transactions on Image Processing*, 12(3):317–327, 2003. 4, 8
- [6] Tony F Chan and Luminita A Vese. Active contours without edges. *IEEE Transactions on image processing*, 10(2):266–277, 2001. 2, 5, 8
- [7] Rachid Deriche and Thierry Blaszk. Recovering and characterizing image features using an efficient model based approach. In *Proceedings of IEEE Conference on Computer Vision and Pattern Recognition*, pages 530–535. IEEE, 1993. 4, 8
- [8] Christopher G Harris, Mike Stephens, et al. A combined corner and edge detector. In *Alvey vision conference*, volume 15, pages 10–5244. Citeseer, 1988. 7, 8
- [9] Erlend Hodneland, Xue-Cheng Tai, and Hans-Hermann Gerdes. Four-color theorem and level set methods for watershed segmentation. *International Journal of Computer Vision*, 82(3):264–283, 2009. 8
- [10] Kun Huang, Yifan Wang, Zihan Zhou, Tianjiao Ding, Shenghua Gao, and Yi Ma. Learning to parse wireframes in images of man-made environments. In *Proceedings of the IEEE Conference on Computer Vision and Pattern Recognition*, pages 626–635, 2018. 8
- [11] Brad Jackson, Jeffrey D Scargle, David Barnes, Sundararajan Arabhi, Alina Alt, Peter Gioumoussis, Elyus Gwin, Paungkaew Sangtrakulcharoen, Linda Tan, and Tun Tao Tsai. An algorithm for optimal partitioning of data on an interval. *IEEE Signal Processing Letters*, 12(2):105–108, 2005. 4, 5
- [12] Diederik P Kingma and Jimmy Ba. Adam: A method for stochastic optimization. *arXiv preprint arXiv:1412.6980*, 2014. 6
- [13] Chunming Li, Chenyang Xu, Changfeng Gui, and Martin D Fox. Level set evolution without re-initialization: a new variational formulation. In *2005 IEEE computer society conference on computer vision and pattern recognition (CVPR’05)*, volume 1, pages 430–436. IEEE, 2005. 8
- [14] David G Lowe. Distinctive image features from scale-invariant keypoints. *International journal of computer vision*, 60(2):91–110, 2004. 8, 17
- [15] D. Martin, C. Fowlkes, D. Tal, and J. Malik. A database of human segmented natural images and its application to evaluating segmentation algorithms and measuring ecological statistics. In *Proc. 8th Int’l Conf. Computer Vision*, volume 2, pages 416–423, July 2001. 1, 5, 6, 7
- [16] Jiri Matas, Ondrej Chum, Martin Urban, and Tomas Pajdla. Robust wide-baseline stereo from maximally stable extremal regions. *Image and vision computing*, 22(10):761–767, 2004. 17
- [17] Fabio Metelli. The perception of transparency. *Scientific American*, 230(4):90–99, 1974. 8
- [18] Krystian Mikolajczyk, Tinne Tuytelaars, Cordelia Schmid, Andrew Zisserman, Jiri Matas, Frederik Schaffalitzky, Timor Kadir, and Luc Van Gool. A comparison of affine region detectors. *International journal of computer vision*, 65(1-2):43–72, 2005. 17
- [19] Suvadip Mukherjee and Scott T Acton. Region based segmentation in presence of intensity inhomogeneity using legendre polynomials. *IEEE Signal Processing Letters*, 22(3):298–302, 2014. 15
- [20] Karl Rohr. Recognizing corners by fitting parametric models. *International journal of computer vision*, 9(3):213–230, 1992. 8
- [21] Carsten Rother, Vladimir Kolmogorov, and Andrew Blake. “GrabCut” interactive foreground extraction using iterated graph cuts. *ACM transactions on graphics (TOG)*, 23(3):309–314, 2004. 2
- [22] Ethan Rublee, Vincent Rabaud, Kurt Konolige, and Gary Bradski. ORB: An efficient alternative to SIFT or SURF. In *2011 International conference on computer vision*, pages 2564–2571. Ieee, 2011. 2, 17
- [23] Daniel Scharstein, Heiko Hirschmuller, York Kitajima, Greg Krathwohl, Nera Nesic, Xi Wang, and Porter Westling. High-resolution stereo datasets with subpixel-accurate ground truth. In *German conference on pattern recognition*, pages 31–42. Springer, 2014. 16
- [24] Luminita A Vese and Tony F Chan. A multiphase level set framework for image segmentation using the mumford and shah model. *International journal of computer vision*, 50(3):271–293, 2002. 5, 8
- [25] Gui-Song Xia, Julie Delon, and Yann Gousseau. Accurate junction detection and characterization in natural images. *International journal of computer vision*, 106(1):31–56, 2014. 8
- [26] Saining Xie and Zhuowen Tu. Holistically-nested edge detection. In *Proc. ICCV*, 2015. 2, 7, 8
- [27] Li Xu, Cewu Lu, Yi Xu, and Jiaya Jia. Image smoothing via L_0 gradient minimization. In *Proceedings of the 2011 SIGGRAPH Asia Conference*, pages 1–12, 2011. 2, 7, 18
- [28] Nan Xue, Gui-Song Xia, Xiang Bai, Liangpei Zhang, and Weiming Shen. Anisotropic-scale junction detection and matching for indoor images. *IEEE Transactions on Image Processing*, 27(1):78–91, 2017. 2, 7, 8

Supplemental Material: Field of Junctions

S1. Additional results on photographs

Figure S1 shows additional results of boundary-aware smoothing and boundary detection on photographs from BSD [15], extending Figure 1.

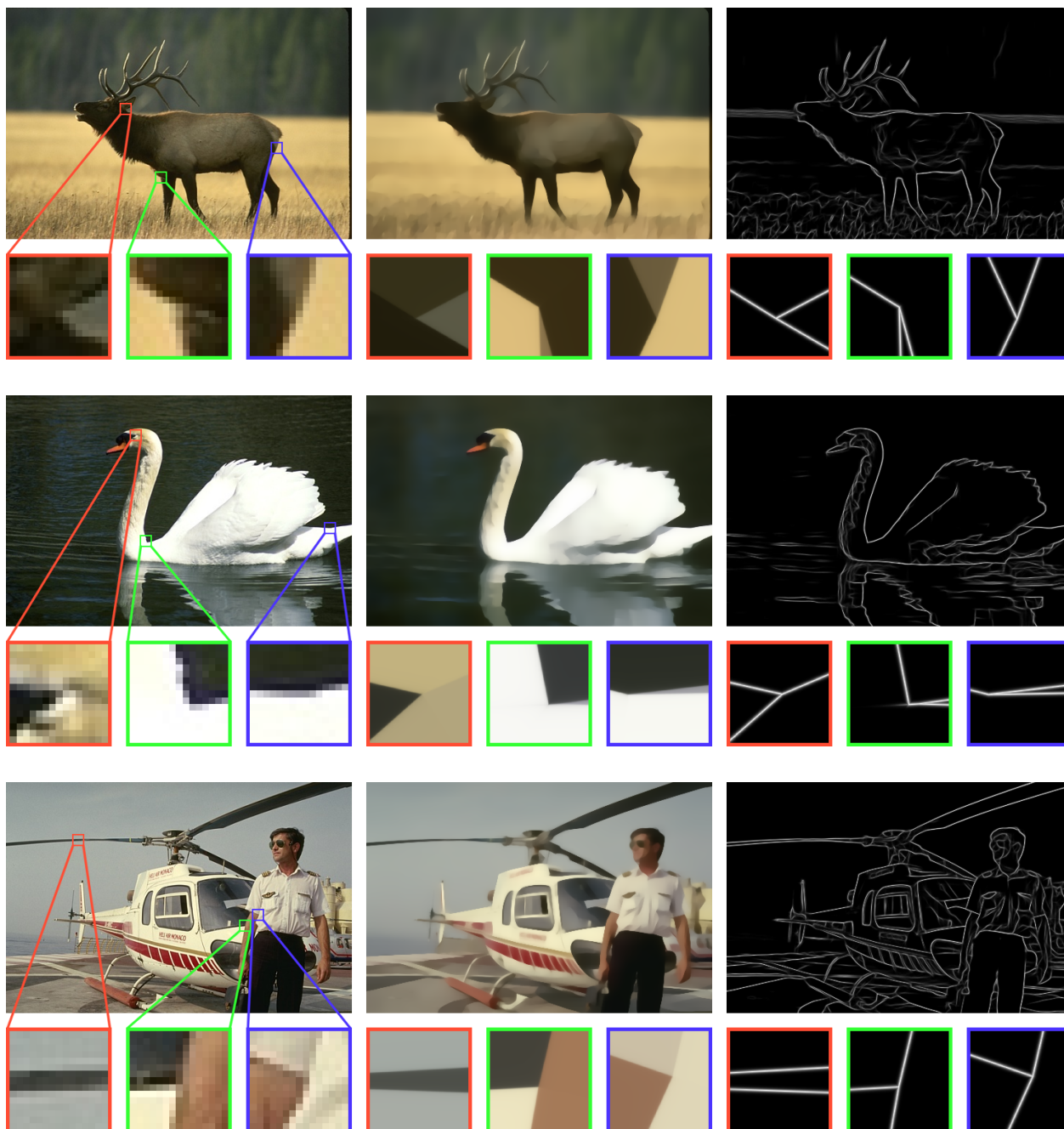


Figure S1

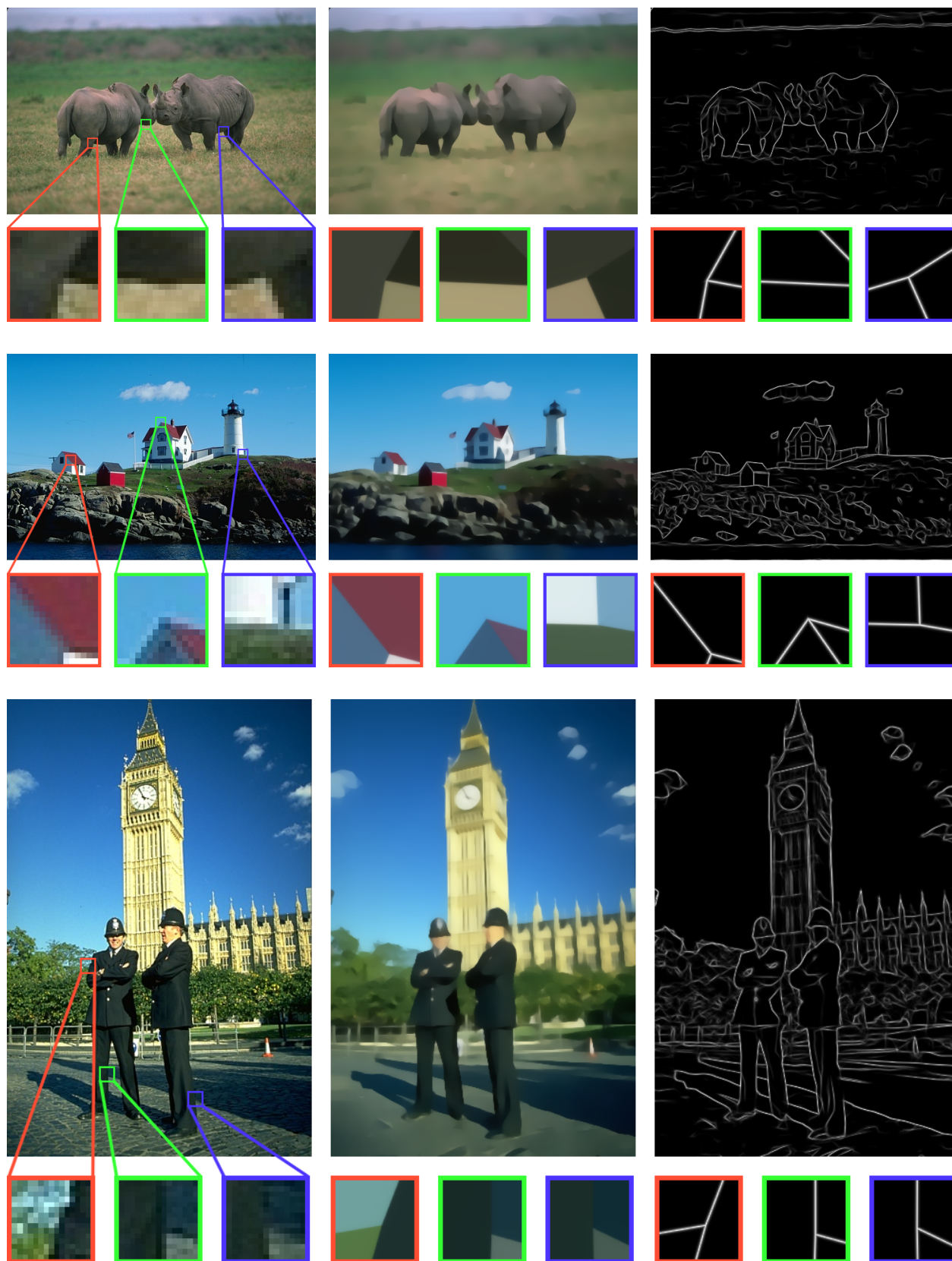


Figure S1: (cont.)

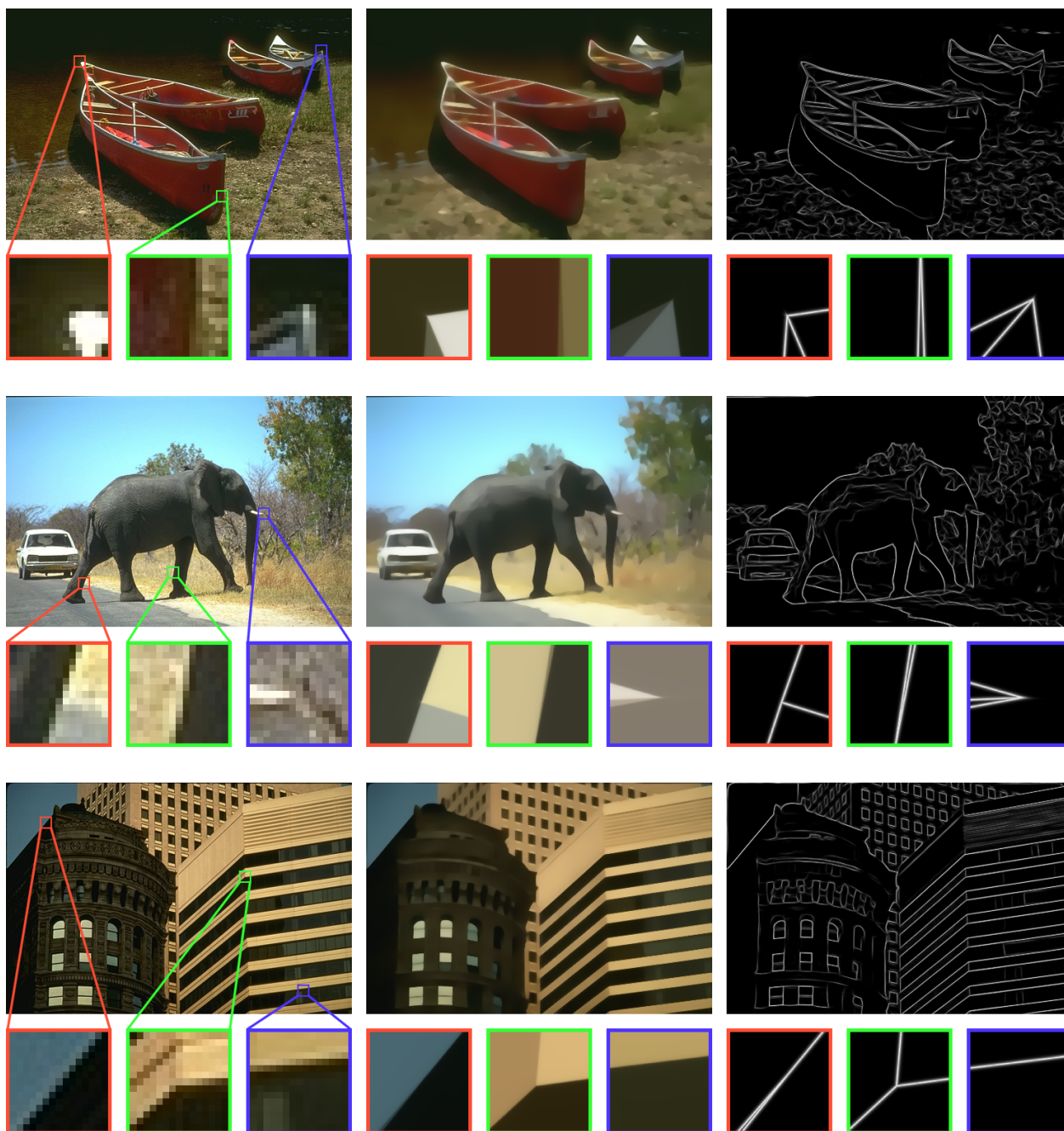


Figure S1: (*cont.*)

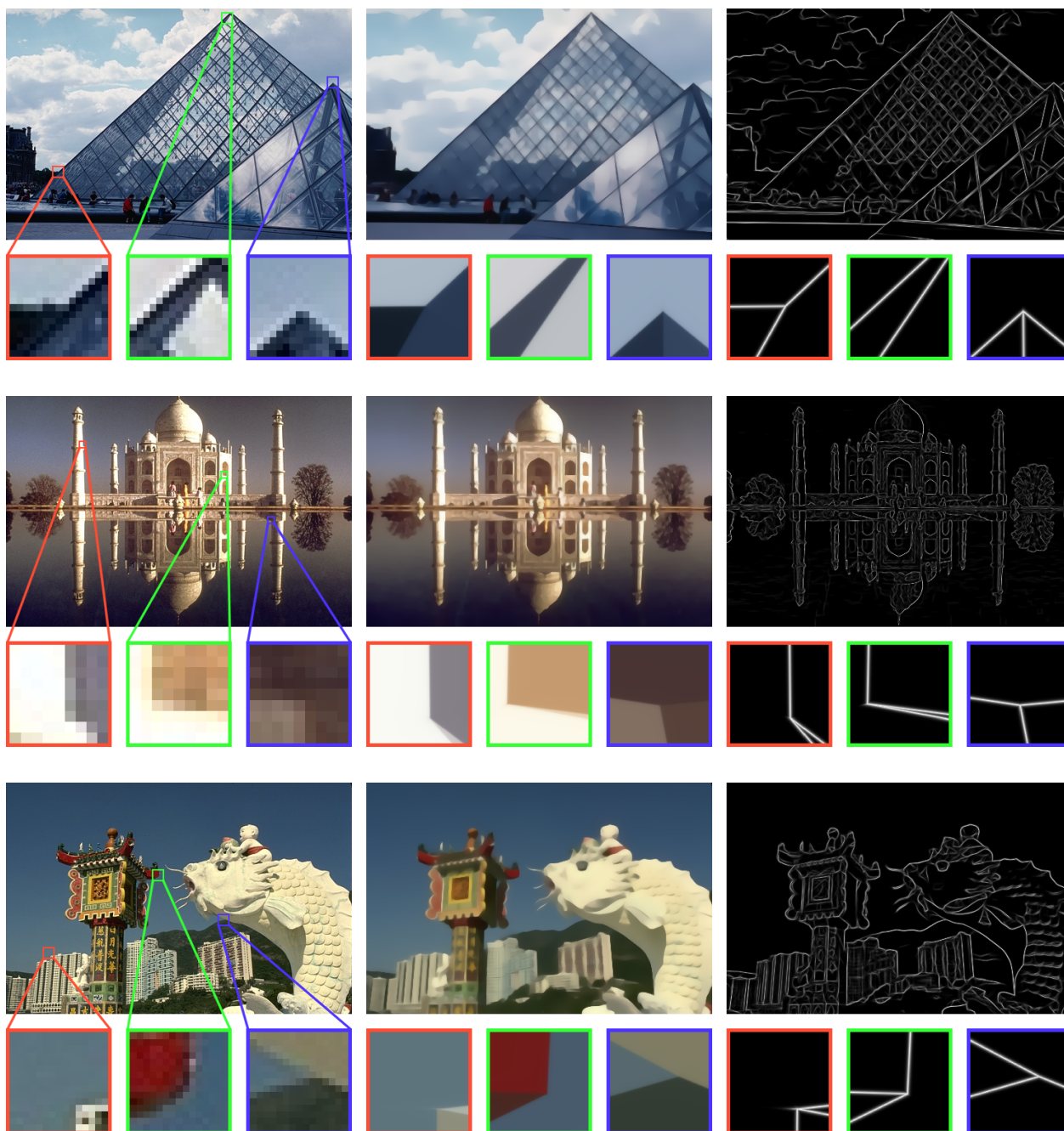


Figure S1: (cont.)

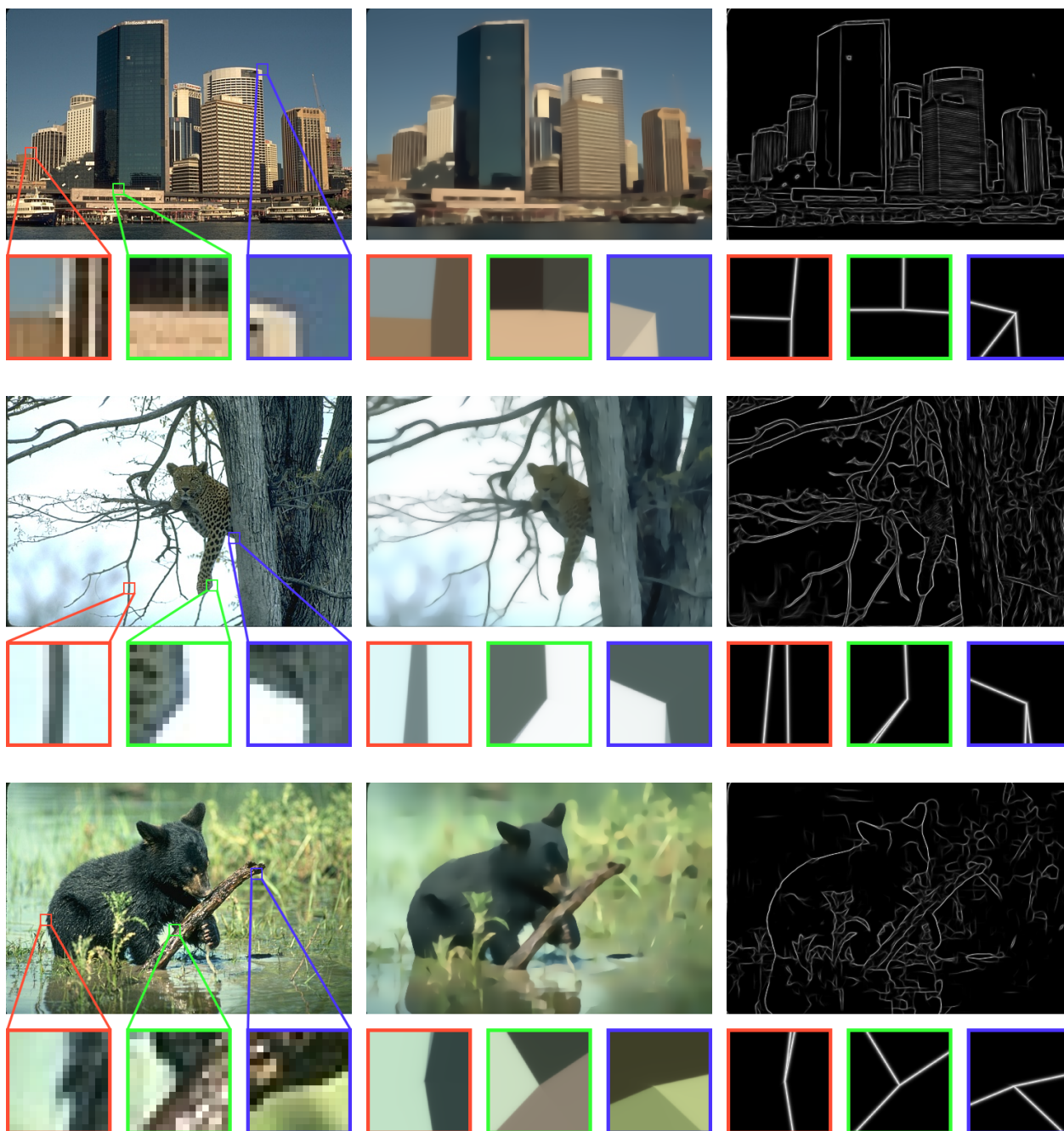


Figure S1: (cont.) Additional results on photographs from BSD.

S2. Additional comparisons with increasing noise

Figure S2 provides an extended comparison of our method to previous methods, extending Figure 2 from the main paper. Here we gradually increase the noise level of the input image, showing the noise level at which each existing method breaks.

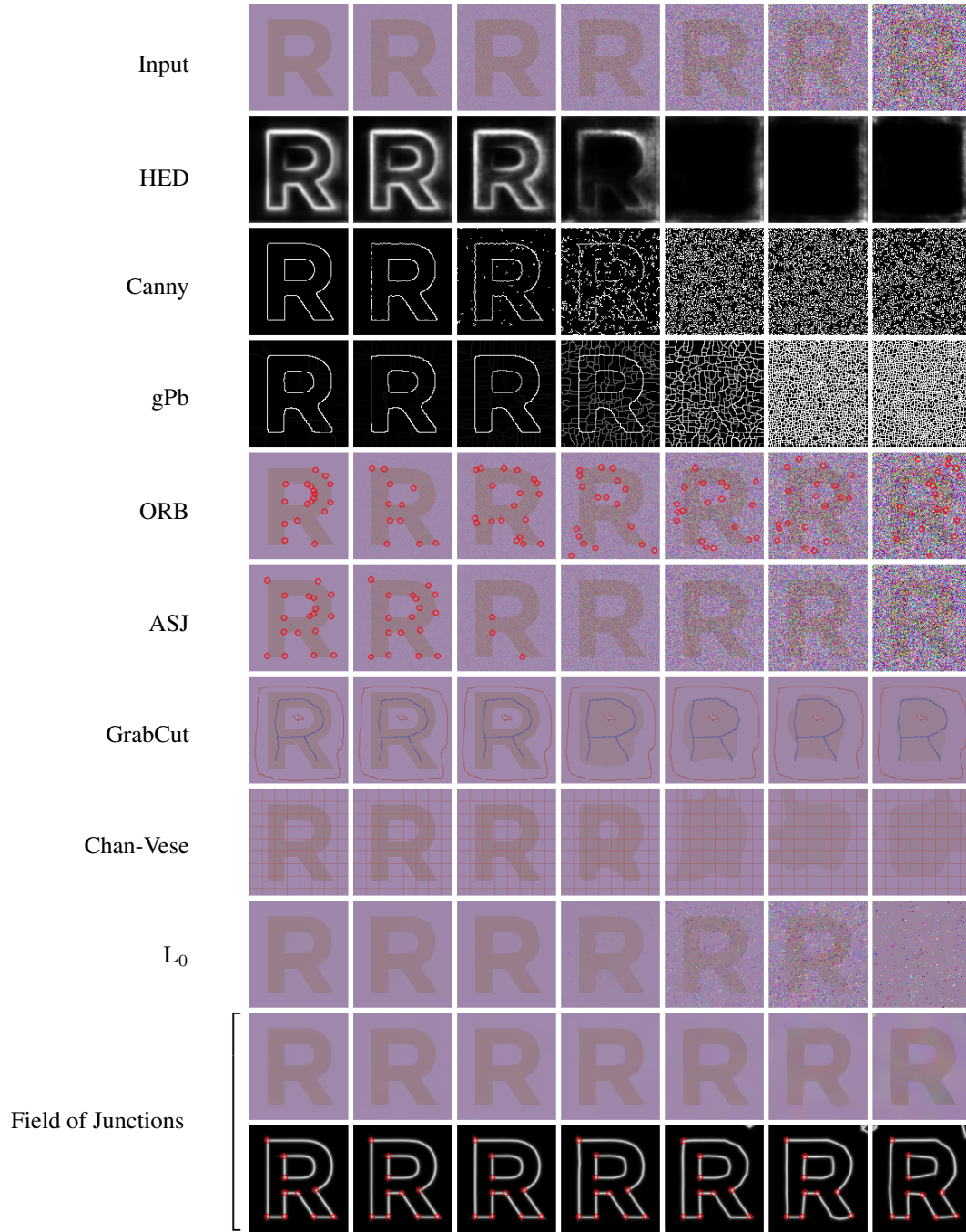


Figure S2: Analyzing the same image at multiple noise levels. From top to bottom: input image, boundary maps from edge detectors (HED, Canny, gPb); detections of corners or junctions superimposed on the input (ORB, ASJ); binary segmentations using manual initialization shown with thin lines (GrabCut, Chan-Vese) or without manual initialization (L_0); and output from the field of junctions. Existing approaches fail in the high noise regime, but the field of junctions does not.

Figure S3 provides a comparison of our method to previous methods on patches from the Smartphone Image Denoising Dataset (SIDD) [1] captured at decreasing light levels.

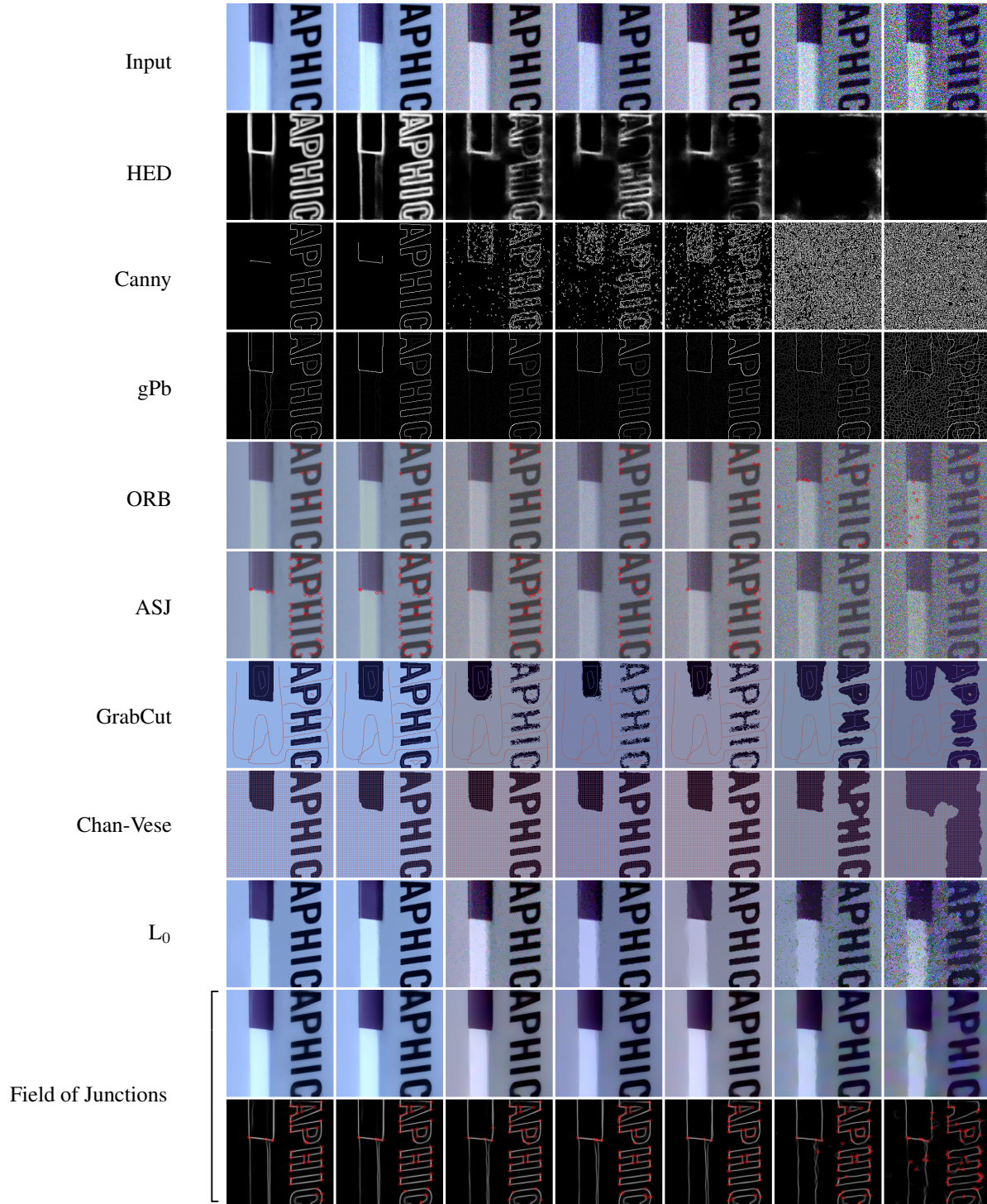


Figure S3: Analyzing the same scene at multiple light levels. Images are taken from SIDD. (The images are displayed at lower contrast in the rows corresponding to ORB and ASJ for clarity.)

S3. Complete proof of Theorem 1

We present a complete proof of Theorem 1 from the main paper, showing that Algorithm 1 is guaranteed to find the M true angles of an image (or image patch) $I(\mathbf{x})$ containing a single junction, in the noiseless case, and when the vertex position is known. For completeness we begin by restating the theorem, omitting the patch index i for convenience:

Theorem 1. *For a junction image $I(\mathbf{x})$ with no noise (i.e., $n \equiv 0$ in Eq. 1 of the main paper) and with vertex $\mathbf{x}^{(0)}$ known, Algorithm 1 is guaranteed to find the globally optimal angles ϕ .*

We begin by first proving a lemma:

Lemma 1. *Define $L(\phi) \triangleq \int_{a(\phi)}^{b(\phi)} w(\phi') \|I(\phi') - c^*(\phi)\|^2 d\phi'$, where $a, b, w: [0, 2\pi) \rightarrow \mathbb{R}$ and $I, c^*: [0, 2\pi) \rightarrow \mathbb{R}^K$ are functions such that $c^*(\phi) \int_{a(\phi)}^{b(\phi)} w(\phi') d\phi' = \int_{a(\phi)}^{b(\phi)} w(\phi') I(\phi') d\phi'$. Then we have:*

$$\frac{d}{d\phi} L(\phi) = w(b(\phi)) \|I(b(\phi)) - c^*(\phi)\|^2 \frac{d}{d\phi} b(\phi) - w(a(\phi)) \|I(a(\phi)) - c^*(\phi)\|^2 \frac{d}{d\phi} a(\phi). \quad (\text{S1})$$

Proof. Using the Leibniz integral rule we have the desired equality plus an additional term:

$$\begin{aligned} & \int_{a(\phi)}^{b(\phi)} w(\phi') \frac{\partial}{\partial \phi} \|I(\phi') - c^*(\phi)\|^2 d\phi' \\ &= -2 \int_{a(\phi)}^{b(\phi)} w(\phi') \frac{d}{d\phi} c^*(\phi) \cdot [I(\phi') - c^*(\phi)] d\phi' \\ &= -2 \frac{d}{d\phi} c^*(\phi) \cdot \int_{a(\phi)}^{b(\phi)} w(\phi') [I(\phi') - c^*(\phi)] d\phi' = 0, \end{aligned} \quad (\text{S2})$$

where the final equality was obtained using the fact that the integral is zero, due to the construction of c^* in the lemma. \square

Lemma 2. *Under the conditions of Theorem 1, the negative log-likelihood function restricted to the j th coordinate $\ell_j(\phi) = \ell(\phi^{(1)}, \dots, \phi^{(j-1)}, \phi, \phi^{(j+1)}, \dots, \phi^{(M)}, x^{(0)}, y^{(0)})$ has no local minima in the open angular interval between any pair of adjacent true angles.*

Proof. The junction image $I(\mathbf{x})$ is radially symmetric around the known vertex $\mathbf{x}^{(0)}$, and therefore we can treat it as an angular function $I(\phi)$ of the angle centered at point $\mathbf{x}^{(0)}$.

From Equation 4 in the main paper, and using polar coordinates relative to the vertex $\mathbf{x}^{(0)}$ we can write the negative log-likelihood:

$$\begin{aligned} \ell(\phi^{(1)}, \dots, \phi^{(M)}, x^{(0)}, y^{(0)}) &= \alpha \sum_{j=1}^M \int_0^{2\pi} \int_0^{R(\phi')} u^{(j)}(\phi') \|I(\phi') - c^{(j)}\|^2 r' dr' d\phi' \\ &= \alpha \sum_{j=1}^M \int_0^{2\pi} \frac{1}{2} R^2(\phi') u^{(j)}(\phi') \|I(\phi') - c^{(j)}\|^2 d\phi' \\ &= \alpha \sum_{j=1}^M \int_{\phi^{(j)}}^{\phi^{(j+1)}} \frac{1}{2} R^2(\phi') \|I(\phi') - c^{(j)}\|^2 d\phi', \end{aligned} \quad (\text{S3})$$

where $R(\phi')$ is the distance of each point on the boundary of the $R \times R$ patch at angle ϕ' from the vertex $\mathbf{x}^{(0)}$, and $u^{(j)}(\phi')$ is an angular indicator function returning 1 if $\phi' \in (\phi^{(j)}, \phi^{(j+1)})$ and 0 otherwise (with the index $j+1$ computed modulo M , and assuming without loss of generality that the angles are non-decreasing, $\phi^{(1)} \leq \dots \leq \phi^{(M)}$). The optimal colors $\{c^{(j)}\}$ are given using Equation 3 in the main paper, or in polar coordinates:

$$c^{(j)} = \frac{\int_0^{2\pi} \int_0^{R(\phi')} u^{(j)}(\phi') I(\phi') r' dr' d\phi'}{\int_0^{2\pi} \int_0^{R(\phi')} u^{(j)}(\phi') r' dr' d\phi'} = \frac{\int_{\phi^{(j)}}^{\phi^{(j+1)}} R^2(\phi') I(\phi') d\phi'}{\int_{\phi^{(j)}}^{\phi^{(j+1)}} R^2(\phi') d\phi'}. \quad (\text{S4})$$

By applying Lemma 1 to Equation S3 and discarding all terms that do not depend on $\phi^{(j)}$, the partial derivative of the negative log-likelihood function with respect to the j th angle in any open interval between two true angles is:

$$\frac{d}{d\phi} \ell_j(\phi) = \frac{1}{2} \alpha R^2(\phi) \left[\|I(\phi) - c^{(j-1)}\|^2 - \|I(\phi) - c^{(j)}\|^2 \right]. \quad (\text{S5})$$

We finish proving the lemma by contradiction. Let us assume ϕ is a local minimum point of ℓ_j in the open interval between a pair of true angles. Because ℓ_j is smooth within any such interval, we have $\frac{d}{d\phi} \ell_j(\phi) = 0$, and from Equation S5 we have:

$$\|I(\phi) - c^{(j-1)}\|^2 - \|I(\phi) - c^{(j)}\|^2 = 0. \quad (\text{S6})$$

Using this expression with the derivative of Equation S5 we obtain that the second derivative at the local minimum is:

$$\begin{aligned} \frac{d^2}{d^2\phi} \ell_j(\phi) &= \alpha R^2(\phi) \left\{ \left[\frac{d}{d\phi} I(\phi) - \frac{d}{d\phi} c^{(j-1)} \right] \cdot [I(\phi) - c^{(j-1)}] - \left[\frac{d}{d\phi} I(\phi) - \frac{d}{d\phi} c^{(j)} \right] \cdot [I(\phi) - c^{(j)}] \right\} \\ &= \alpha R^2(\phi) \left\{ -\frac{d}{d\phi} c^{(j-1)} \cdot [I(\phi) - c^{(j-1)}] + \frac{d}{d\phi} c^{(j)} \cdot [I(\phi) - c^{(j)}] \right\}, \end{aligned} \quad (\text{S7})$$

where we used the fact that $I(\phi)$ is constant for every ϕ in an open interval between two true angles.

Multiplying both sides of Equation S4 by the denominator of the right hand side for indices $j-1$ and j and differentiating with respect to ϕ yields:

$$\begin{aligned} \frac{d}{d\phi} c^{(j-1)} \int_{\phi^{(j-1)}}^{\phi} R^2(\phi') d\phi' + c^{(j-1)} R^2(\phi) &= R^2(\phi) I(\phi), \\ \frac{d}{d\phi} c^{(j)} \int_{\phi}^{\phi^{(j)}} R^2(\phi') d\phi' - c^{(j)} R^2(\phi) &= -R^2(\phi) I(\phi). \end{aligned} \quad (\text{S8})$$

Rearranging we obtain:

$$R^2(\phi) [I(\phi) - c^{(j-1)}] = \frac{d}{d\phi} c^{(j-1)} \int_{\phi^{(j-1)}}^{\phi} R^2(\phi') d\phi', \quad (\text{S9})$$

$$R^2(\phi) [I(\phi) - c^{(j)}] = -\frac{d}{d\phi} c^{(j)} \int_{\phi}^{\phi^{(j)}} R^2(\phi') d\phi'. \quad (\text{S10})$$

Finally, we substitute Equations S9 and S10 into the expression for the second derivative in Equation S7:

$$\frac{d^2}{d^2\phi} \ell_j(\phi) = \alpha \left\{ -\left\| \frac{d}{d\phi} c^{(j-1)} \right\|^2 \int_{\phi^{(j-1)}}^{\phi} R^2(\phi') d\phi' - \left\| \frac{d}{d\phi} c^{(j)} \right\|^2 \int_{\phi}^{\phi^{(j)}} R^2(\phi') d\phi' \right\}, \quad (\text{S11})$$

and the second derivative at ϕ is negative, which is contradictory to our assumption that ϕ is a minimum point, thus concluding our proof of the lemma. \square

The complete proof of Theorem 1 is then obtained by using Lemma 2 and the proof sketch from the main paper:

Proof. First, note that $\ell_j(\phi)$ is continuous and smooth for all ϕ other than possibly a discontinuity in the derivative at any of the true junction angles. If the optimal ϕ is not one of the true junction angles then it must lie in the *open* interval between two such angles, i.e. $\phi \in (\phi^-, \phi^+)$. From Lemma 2 we have that $\ell_j(\phi)$ does not have any local minima in (ϕ^-, ϕ^+) , and therefore for each angular interval between two true junction angles the cost function must be minimized at one of the endpoints. Therefore repeatedly minimizing $\ell_j(\phi)$ for $j = 1, \dots, M$ is guaranteed to provide a globally optimal set of angles $\{\phi^{(1)}, \dots, \phi^{(M)}\}$. \square

S4. Complete specification of vertex detector

The vertex probability for each pixel $V(\mathbf{x})$ is described in Equation 13 of the main paper. We repeat the expression here with a full explanation of all of its terms. We set:

$$V(\mathbf{x}) = \sum_{i=1}^N w_i \kappa \left(\mathbf{x} - \mathbf{x}_i^{(0)} \right), \quad (\text{S12})$$

$$\kappa(\Delta \mathbf{x}) = \exp \left(-\frac{\|\Delta \mathbf{x}\|^2}{2\gamma_1^2} \right), \quad (\text{S13})$$

$$w_i = \exp \left(-\frac{\|\mathbf{x}_i^{(0)} - \mathbf{p}_i\|^2}{2\gamma_2^2} \right) \cdot \max_{k \neq l} \min \left\{ 1, \left[1 + \cos \left(\phi^{(k)} - \phi^{(l)} \right) \right] \left[1 - \left| \cos \left(\phi^{(k)} - \phi^{(l)} \right) \right| \right]^{\gamma_3} \right\}, \quad (\text{S14})$$

where \mathbf{p}_i is the position of the center of the i th patch and $\gamma_1, \gamma_2, \gamma_3$ are parameters.

Each weight w_i is composed of two terms, such that a junction only contributes to the detector if its vertex position is sufficiently close to the center of the patch, and at least a pair of its wedges has an angle not too close to 0 or π . The first term is simply a Gaussian term in the distance from the vertex to the patch center, and the second is a function that returns 1 if any of the junction's wedges has an angle close to $\pi/2$ and drops to 0 if all angles are 0 or π . The second term is chosen to be asymmetric around $\pi/2$ since angles larger than $\pi/2$ are more likely to be caused by structure in the image with nonzero curvature than those below $\pi/2$, and thus should have a lower weight. In all experiments in our paper we use $\gamma_1 = 2R$, $\gamma_2 = R/2$, $\gamma_3 = 2$.

S5. Importance of refinement step

Figure S4 shows a comparison of the results obtained by a field of junctions with and without the refinement step on a photograph from BSD. In natural images with low noise, the refinement step mainly cleans up the boundary maps, only maintaining boundaries corresponding to salient edges and junctions in the image. Because the main effect of the refinement step in this case is to remove unnecessary boundaries around uniform regions of the image, it does not affect the boundary-aware smoothing, as the pixel colors predicted in both cases are similar.

Figure S5 shows the effect of the refinement step over multiple noise levels. While in the low-noise regime the refinement step of our algorithm only suppresses superfluous boundaries, in the high-noise regime the spatial consistency enforced by it also significantly improves the boundaries predicted by each junction.

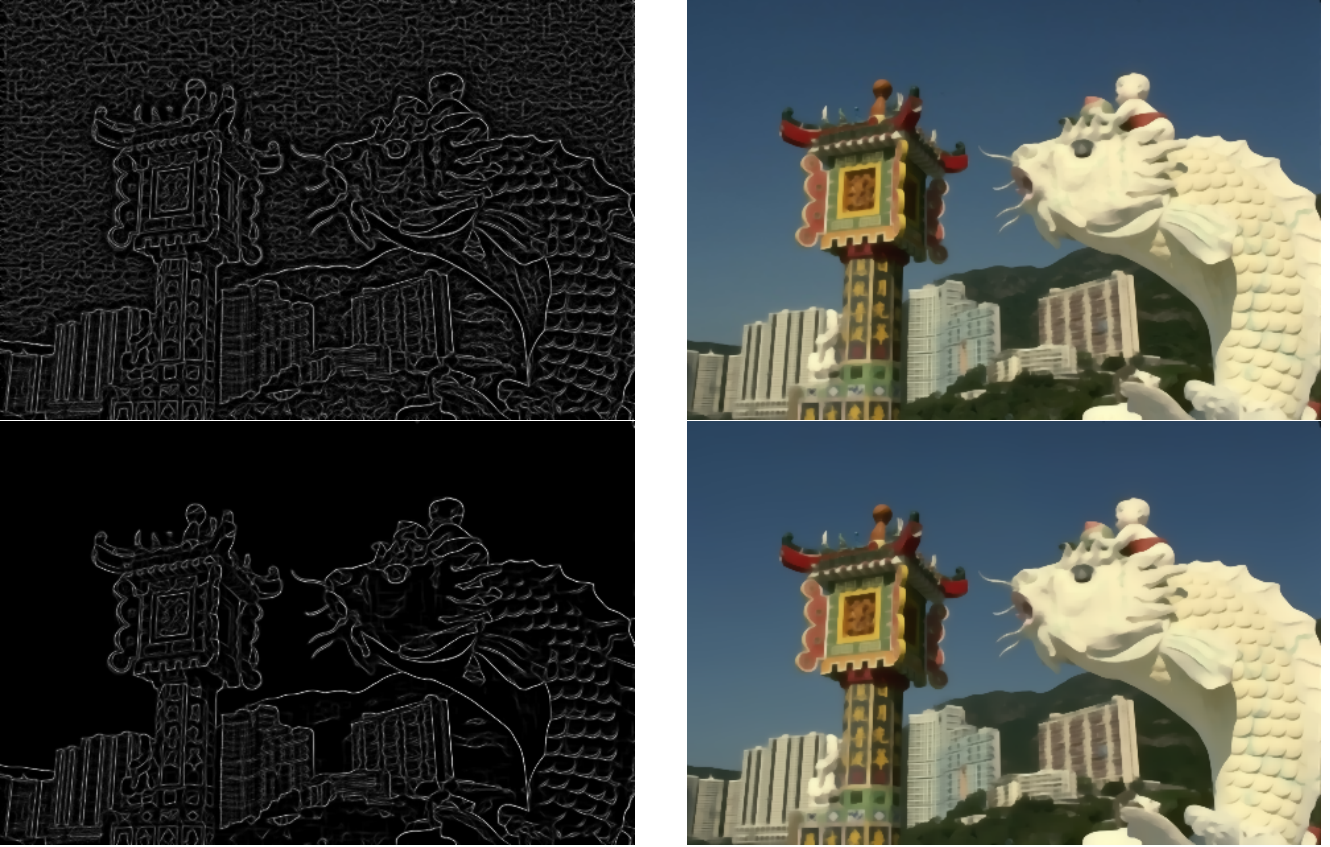


Figure S4: Comparison of our model without the refinement step (top) and with it (bottom). The refinement step improves the boundary map by suppressing boundaries in uniform regions and preventing additional spurious boundaries. In the low-noise regime the refinement step does not significantly impact the boundary-aware smoothing result, meaning that smoothing using a field of junctions can be accelerated significantly by omitting the refinement step.



Figure S5: Field of junctions obtained with the refinement step of our algorithm (middle row) and without it (bottom row), on a synthetic image with increasing noise levels. The refinement step reduces superfluous boundaries across all noise levels, and significantly improves the prediction near true boundaries in the high-noise regime.

S6. Dataset

Figure S6 shows representative images selected from our synthetic dataset. Our dataset is designed to provide control over noise levels and allow access to the ground truth edges and vertices, so that accurate quantitative analysis can be made. Our dataset contains patches that our field of junctions can handle exactly (uniformly-colored regions, edges, corners, and junctions), as well as ones that it can only model approximately (curved edges, curved junctions, *etc.*).

Our dataset contains 300 grayscale images, 100 of each of three types:

1. Images containing two curved objects of gray levels 128 and 255 on a black background (see Figure S6a).
2. Images containing two rotated squares of gray levels 128 and 255 on a black background (see Figure S6b).
3. Images containing 4 regions of gray levels 0, 85, 170, and 255 separated by two 3-junctions (see Figure S6c).

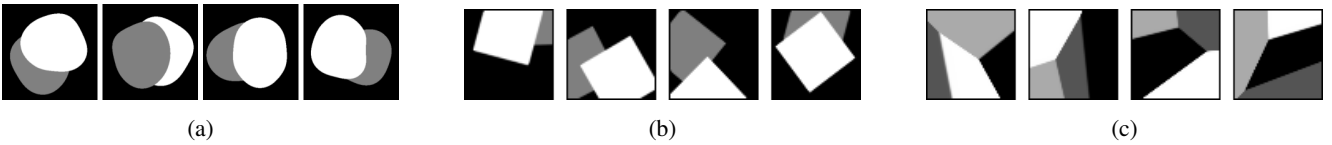


Figure S6: Images from our synthetic dataset.

S7. Comparison with the 4-junction model

In our main paper all experiments are done using the 3-junction model (*i.e.* we set $M = 3$). The 4-junction model ($M = 4$) described in the paper provides an advantage only in certain applications which tend to contain X-junctions. Some examples for such cases are images containing semi-transparent objects, reflections from transparent ones, or specific textures such as the checkerboard in Figure 9 in the main paper.

Figure S7 shows a comparison of a field of junctions obtained with our $M = 3$ model with that obtained by our $M = 4$ model. The differences between the two are usually insignificant in photographs, since those typically do not contain many salient X-junctions.

Figures S8 and S9 show a comparison of the two models over images with increasing noise levels. In images not containing X-junctions both models perform similarly, with the 3-junction model slightly outperforming the 4-junction model at very high noise levels. Because the 4-junction model contains an additional angle it tends to either output more superfluous boundaries than the 3-junction model (as in Figure S9), or in some cases less of them (as in Figure S8).



Figure S7: Boundary maps obtained by our field of junctions using the 3-junction and 4-junction models. The boundary maps obtained from the input image (left) using $M = 3$ and $M = 4$ are plotted (right) in the red and green channels respectively. Salient boundaries generally appear yellow, corresponding to a perfect agreement between the two models. Some boundaries appear green, corresponding to ones predicted only by the 4-junction model, which tends to suppress small-scale details less than the 3-junction one.



Figure S8: Boundary maps obtained using the 3-junction and 4-junction models on a synthetic image under increasing noise. At low noise both models produce similar results, but at very high noise, the 3-junction model performs slightly better.

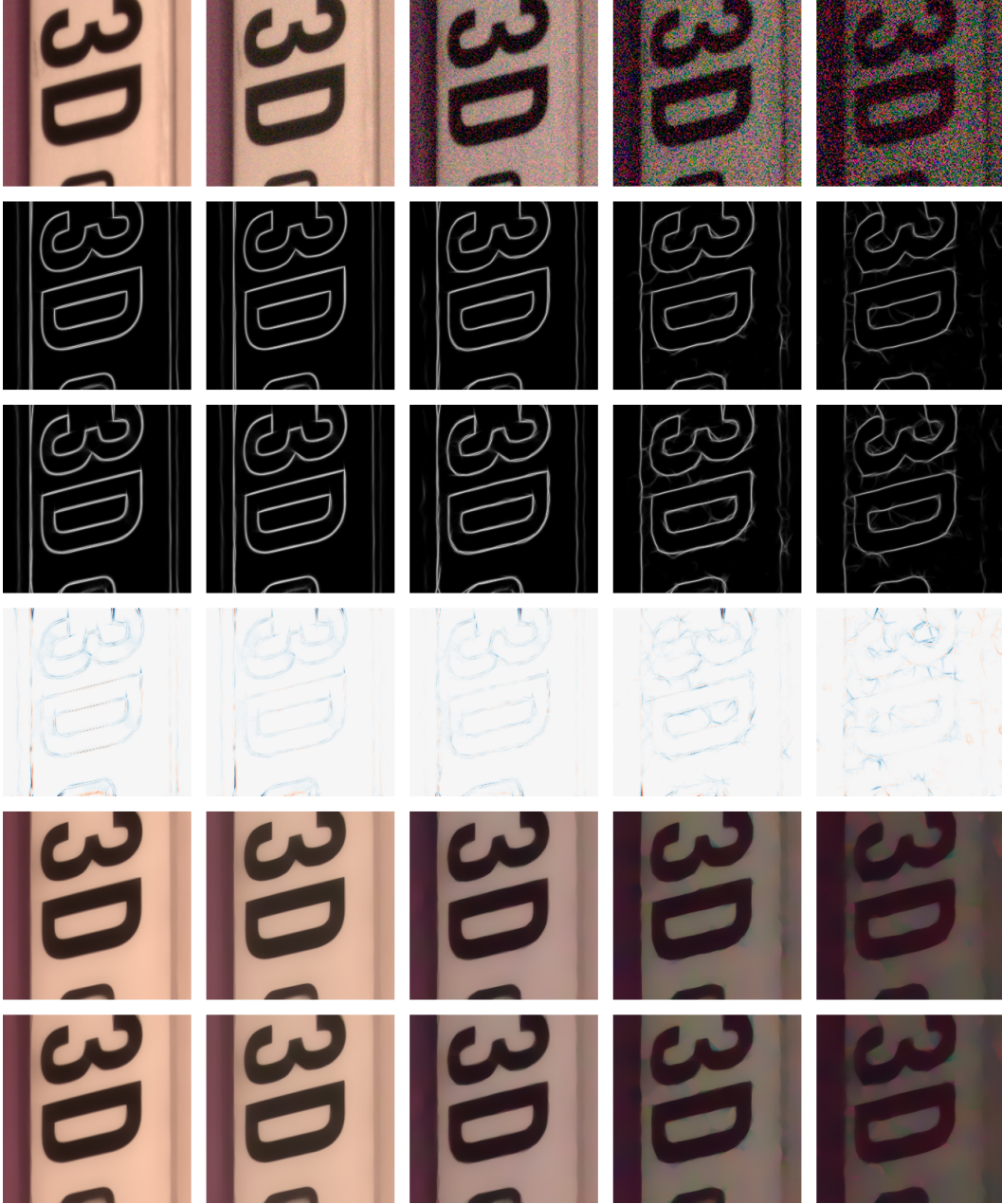


Figure S9: Boundary maps obtained using the 3-junction and 4-junction models on images from SIDD. The boundary maps output by the 4-junction model (2nd row) are similar to those output by the 3-junction model (3rd row), but typically contain more boundaries. The difference between the two boundary maps is shown in the 4th row, where blue pixels are those predicted as boundaries by the 4-junction model and not by the 3-junction model, and red pixels correspond to the opposite case. The boundary-aware smoothing results (using $M = 3$ in 5th row, $M = 4$ in 6th row) are not significantly affected by the number of angles.

S8. Comparison with the linear color model

In our main paper all experiments are done using the constant color model. The linear color model described in the paper outperforms the constant color model in specific applications. An example for such an application is when the images contain large regions with linear color. Figure S10 shows an example for this type of image. Our linear color model perfectly explains the image, while the constant color model provides a number of additional low-confidence boundaries throughout the image.

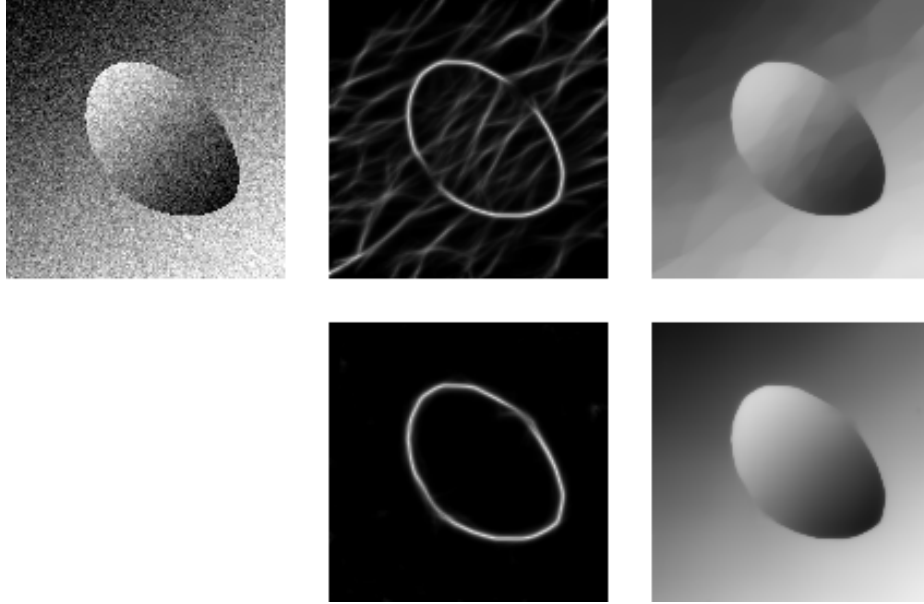


Figure S10: Field of junctions for an image containing linear color regions (left) using the constant color model (top row) compared with the linear color model (bottom row). The linear color model provides a better result in this type of application, but we found the constant color model to be sufficient for the experiments in our paper, and specifically for photographs. Input image taken from [19].

S9. Application to RGB-D images

In our main paper all experiments are done using grayscale ($K = 1$) or RGB images ($K = 3$). We find that our field of junctions is also useful for RGB-D images ($K = 4$), allowing recovery of missing depth values from datasets such as the Middlebury Stereo Dataset [23]. Figure S11 shows the depth values obtained by first analyzing an image into its field of junctions, ignoring pixels with missing depth values, and using the 4-channel coloring functions $\{c_i^{(j)}\}$ to compute the boundary-aware smoothing of the input RGB-D image using Equation 14 in the main paper.



Figure S11: Analyzing an image into its field of junctions can be used for filling missing depth values in stereo datasets such as Middlebury. The input RGB image (left) and depth map with missing values (center) are analyzed into their 4-channel field of junctions. The depth channel of the resulting boundary-aware smoothed RGB-D image (right) smoothly fills the missing values.

S10. Repeatability over change in viewpoint

We test the repeatability of our vertex detector with respect to change in viewpoint using the Graffiti dataset of [18], which includes images of a planar surface from angles of 20 degrees to 60 degrees. Figure S12 shows the repeatability of our vertex detector compared to that of other interest point detectors, as well as the output of our vertex detector on three of the images in the dataset.

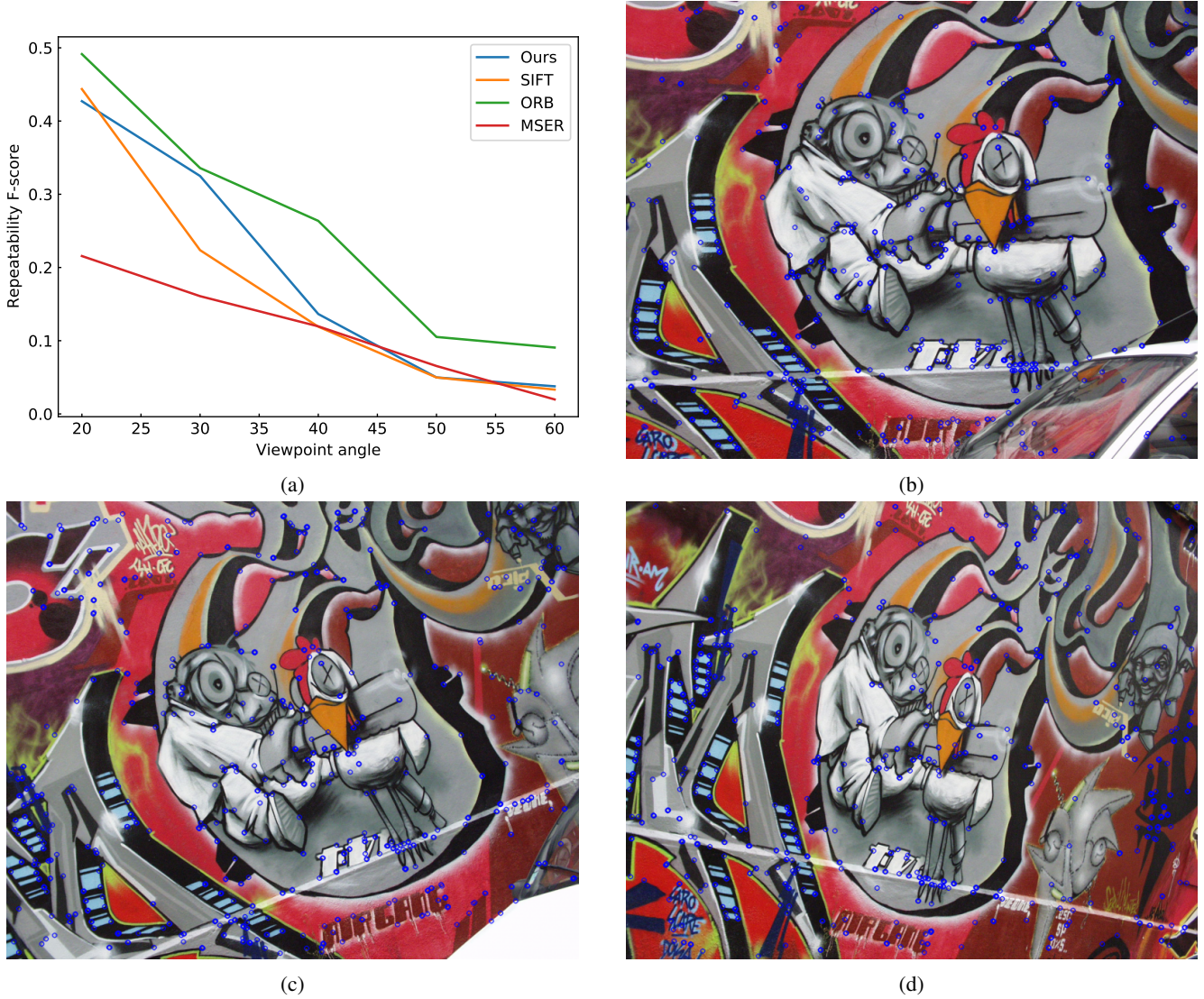


Figure S12: Comparison of repeatability over viewpoint on the “Graffiti” scene from [18]. (a) A comparison of our vertex detector with SIFT [14], ORB [22], and MSER [16]; (b-d) Examples of our vertex detector’s output in images captured at the frontal view and at viewing angles 20 and 30 degrees. Our repeatability is comparable to other popular interest point detectors.

S11. Comparison with L_0 smoothing

Figure S13 shows a comparison of our boundary-aware smoothing results with those obtained by L_0 smoothing [27]. Each method has a single parameter controlling the level of detail. Our method also has a parameter for selecting the spatial size of the details in the smoothed image (see for example the smoothed details inside the structure in the bottom example of Figure S13).

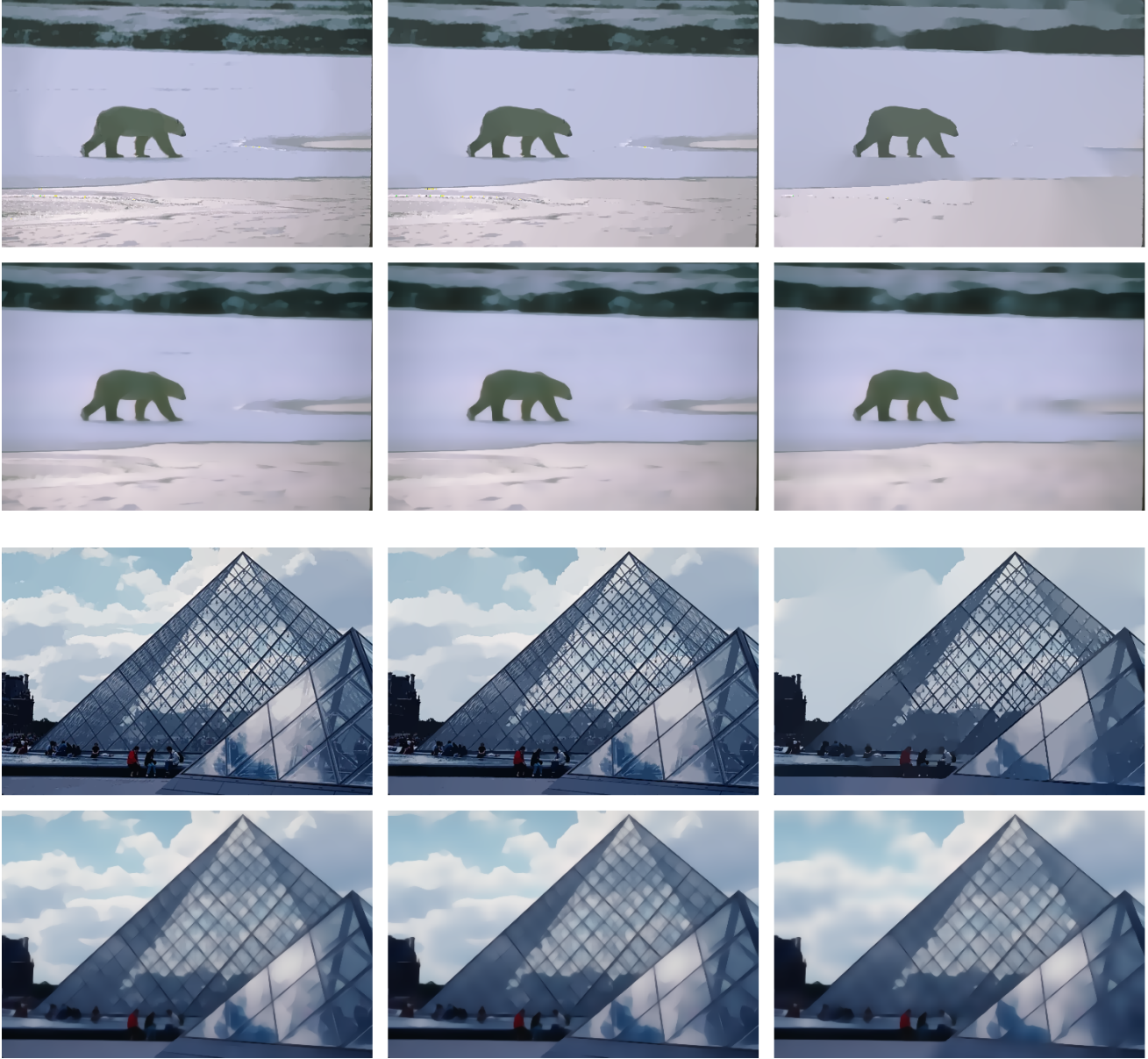


Figure S13: The smoothed results obtained by L_0 smoothing (top row of each example) compared to our boundary-aware smoothing (bottom row). The smoothing parameter is increased from left to right for both methods.